Geophysical Journal International

Geophys. J. Int. (2016) **204,** 215–235
GJI Seismology

doi: 10.1093/gji/ggv441

Seismic evidence for lithospheric modification associated with intracontinental volcanism in Northeastern China

Dou Kang,[1] Weisen Shen,[2] Jieyuan Ning[1] and Michael H. Ritzwoller[2]

[1] *Institute of Theoretical and Applied Geophysics, School of Earth and Space Sciences, Peking University, Beijing* 100871, *China*
[2] *Department of Physics, University of Colorado at Boulder, Boulder, CO* 80309, *USA. E-mail: Weisen.Shen@colorado.edu*

Accepted 2015 October 9. Received 2015 October 8; in original form 2015 May 9

SUMMARY

Using data predominantly from the NECESS Array, but also incorporating surface wave data from surrounding networks, we present the results of a Bayesian Monte Carlo inversion of receiver functions, Rayleigh wave ellipticity (H/V ratio) and Rayleigh wave group and phase speeds from 8 to 80 s period for the 3-D shear velocity structure of the crust and uppermost mantle beneath Northeast China. We define the final model as the mean and standard deviation of the posterior distribution at each location on a 0.5° × 0.5° grid from the surface to 150 km depth. The primary scientific motivation is to investigate the expression of intracontinental volcanism across the region. The model lithosphere displays prominent features (middle and lower crustal velocity, Moho depth, lithospheric thickness) across the study area that coincide with the location of volcanoes, which are predominantly situated in two distinct volcanic regions, which we call the 'Northeast China Lineated Quaternary Volcanic Zone', found near the eastern margin of the Songliao Basin and extending to Changbaishan Volcano, and the 'Northern and Southern Greater Xing'an Range Pleistocene Volcanic Zones'. There is a strong similarity between the lateral distribution of depth-integrated mantle velocity anomalies in our model with the teleseismic body wave model of Tang *et al*., although the vertical distribution of anomalies differ.

Key words: Tomography; Surface waves and free oscillations; Crustal structure; Continental tectonics: extensional; Asia.

1 INTRODUCTION

In a recent study, Shen *et al.* (2015) produced a seismic reference model of shear wave speeds in the crust and uppermost mantle across China, as a continuation and culmination of three earlier studies (Yang *et al.*, 2010, 2012; Zheng *et al.* 2011; Zhou *et al.* 2012). This model, which we refer to here as China_2015, was produced using measurements of Rayleigh wave dispersion alone that derived from ambient noise and earthquake tomography. China_2015 is principally a V_s model and is presented on a 0.5° × 0.5° grid across all of China, extending to a depth of 150 km. The model was generated via a Bayesian Monte Carlo inversion and is defined by the mean and standard deviation of the posterior distribution at each grid node. Such surface wave inversions characterize V_s between discontinuities much better than the depths to interfaces, and Shen *et al.* (2015) present their model (and the group and phase speed maps on which it was derived) specifically to act as the basis for later studies that incorporate data that complement information from surface wave dispersion. The purpose of the present paper is to refine the model of the crust and uppermost mantle in northeastern China beneath the NECESS Array (NorthEast China Extended SeiSmic Array) by introducing two additional types of data: receiver functions (RFs) and Rayleigh wave ellipticity (or H/V ratio). These data provide much tighter constraints on sedimentary and crustal thicknesses than surface wave dispersion alone, which improves depth resolution in the model substantially. To the best of our knowledge, this is the first study to invert surface wave dispersion, RFs and H/V ratio simultaneously.

Our study focuses on the use of data from the NECESS experiment, which deployed 127 temporary broadband seismometers, with the average station spacing of ∼80 km, across Northeast China from September 2009 to August 2011. The array ranges from about 116° to 134°E in longitude and 42° to 48°N in latitude, covering part of the Erlian Basin (ELB), most of the Greater Xing'an Range (GXAR), the Songliao Basin (SLB), the Zhangguangcai Range (ZGCR), the Changbai Mountain Range (CBM), the Sanjiang Basin (SJB) and the Jiamusi Massif, as illustrated in Fig. 1(b). The unprecedented station coverage provided by the NECESS Array (e.g. Tang *et al.* 2014; Tao *et al.* 2014) motivates us to develop multiple seismic data sets to illuminate the seismic structure of the lithosphere in Northeast China. We produce RFs from all 127 stations, while we obtain Rayleigh wave measurement (both dispersion and ellipticity) for 120 stations for which we have instrument response information.

The model we present here is constructed with a joint Bayesian Monte Carlo inversion of Rayleigh wave phase and group

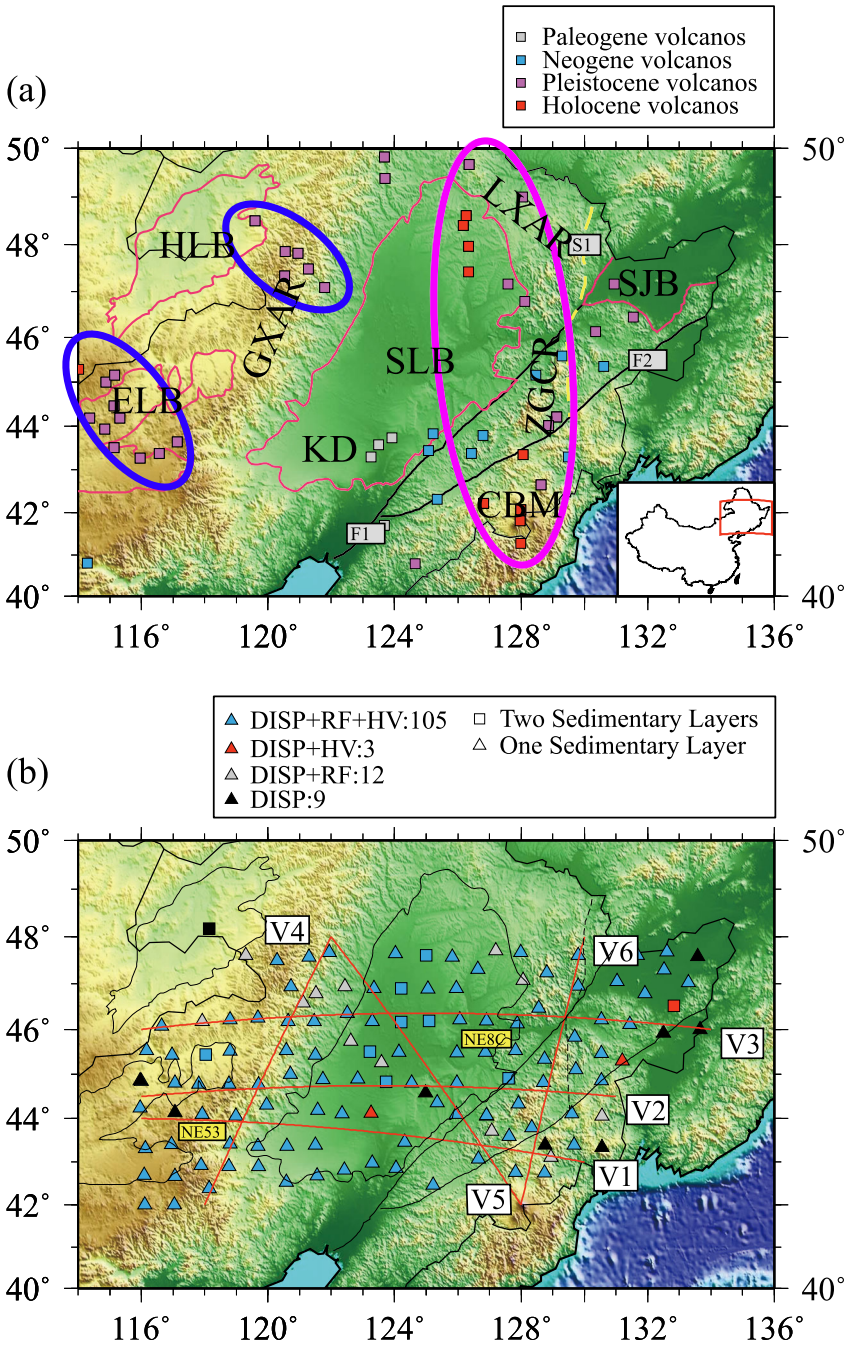

Figure 1. (a) Reference map of geological features, faults and sedimentary basins, displaying the location and age of the principal volcanoes (From Chen *et al.* 2007). Sedimentary basins: ELB—Erlian Basin; HLB—Hailar Basin; SLB—Songliao Basin; SJB—Sanjiang Basin; KD—Kailu Depression. Mountain ranges: GXAR—Greater Xing'an Range; LXAR—Lesser Xing'an Range; ZGCR—Zhangguancai Range; CBM—Changbai Mountain Range. Faults/Sutures: S1 (yellow dashed line)—Jiayin-Mudanjiang Suture; F1—Yilan-Yitong Fault; F2—Dunhua-Mishan Fault. The Jiamusi Massif (not shown) lies east of the Jiayin-Mudanjiang Suture and includes the Sanjiang Basin. Blue ovals: Northern/Southern Greater Xing'an Range Pleistocene Volcanic Zones. Pink oval: Northeast China Lineated Quaternary Volcanic Zone. (b) Station map where symbol colour identifies the data used in the inversion: DISP—Rayleigh wave group and phase speed; HV—Rayleigh wave H/V ratio; RF—receiver functions. Symbol type identifies where sediments are modelled with one (triangles) or two (squares) layers. Locations of vertical transects are identified as V1, . . . , V6, shown in Figs 13–16. Stations NE53 and NE8C are identified.

velocities, RFs and measurements of the period-dependent Rayleigh wave H/V ratio (Lin *et al*. 2012; Lin *et al*. 2014). The surface wave dispersion data are the same as those used by Shen *et al.* (2015) to construct the reference model China_2015. These data include ambient noise and earthquake tomography maps in northeastern China from a wide variety of data sources including the GSN, NECESS, F-Net (in Japan), CEArray and the Korean Seismic Network. The Rayleigh wave dispersion measurements from earthquakes incorporated in that model, however, were actually processed for the present study and we discuss them here at greater length. Shen *et al*. (2015) used measurements, maps and uncertainties of Rayleigh wave phase speed from 30–70 s period derived from the application of Helmholtz tomography and we further add results at 75 and 80 s. We construct the RFs using a revision of the harmonic stripping

method described by Shen *et al*. (2013a,b), where the revision is motivated by the azimuthal content of the RFs in this region. The inversion method we apply is also a straightforward generalization of the method described at length by Shen *et al.* (2013a). Because the data we use overlap the data used to produce the reference model China_2015, in order for a more meaningful comparison we do not use that model as our starting point but rather the earlier model of Zheng *et al.* (2011), which was also the starting point for the reference model China_2015.

Northeast China principally is composed of geological terranes that were amalgamated during the Paleozoic and Mesozoic Eras (Wu *et al*. 2011). The region underwent active intra-continental magmatism and extension during the late Mesozoic era (Ren *et al.* 2002; Wang *et al.* 2006), which led to Basin and Range type fault basins, including the NNE-trending SLB which lies at the centre of our study region (Ren *et al.* 2002; Feng *et al.* 2010; Wei *et al.* 2010). Consensus has yet to be reached regarding the nature of the intraplate volcanism and its relation to deeper geodynamic processes, although various models have been proposed; for example, mantle plume (e.g. Lin *et al.* 1998), backarc extension associated with the subduction and rollback of the Paleo-Pacific plate (e.g. Watson *et al.* 1987; Wei *et al.* 2010) and delamination of the thickened lithosphere after closure of the Mongol–Okhotsk Ocean (e.g. Wang *et al.* 2006; Zhang *et al.* 2010). In the Cenozoic Era, northeastern China experienced several additional episodes of volcanism, which initiated in the Songliao graben and then migrated flankward (Liu *et al.* 2001). The locations and approximate ages of the principal Cenozoic volcanoes in our study region are identified in Fig. 1(a) (Chen *et al.* 2007), where we identify two distinct volcanic regions, which we call the 'Northeast China Lineated Quaternary Volcanic Zone' and the 'Northern and Southern Greater Xing'an Range Pleistocene Volcanic Zones'.

The primary motivation of this study is to investigate the expression of intracontinental volcanism in the crust and uppermost mantle beneath Northeast China. The model we present is not the first model of the crust and uppermost mantle beneath Northeast China. Earlier surface wave models include those of Zheng *et al.* (2011) and Shen *et al.* (2015) as well as others (Huang *et al.* 2003; Zheng *et al.* 2008; Li *et al.* 2012, 2013; Bao *et al.* 2015), and some studies have combined surface wave with other data (Obrebski *et al.* 2012; Guo *et al.* 2015). However, the model presented here possesses several signature novelties. (1) It is based on an extensive surface wave dispersion data set using both ambient noise and earthquake tomography that is equalled only by the study of Shen *et al.* (2015). (2) It incorporates two sources of complementary information about shallow structures as well as depths to interfaces: RFs and Rayleigh wave H/V ratios. (3) The model that we present possesses uncertainty estimates, which we contrast with uncertainty estimates using surface wave data alone to demonstrate the advantage of the new measurements. Finally, we compare our results in the mantle with the teleseismic body wave model of Tang *et al.* (2014), which is also based on the use of NECESS data.

The paper is organized as follows. In Section 2, we discuss the development of the Rayleigh wave phase and group velocity data sets from both ambient noise and earthquake data, the Rayleigh wave H/V data set and the RF data set, including quality control procedures and observational uncertainties. In Section 3, we discuss the inverse problem including model parametrization, the generation of the prior distribution and a detailed assessment of the effect of introducing RFs and H/V data on the posterior distribution. Section 4 discusses the resulting model and uncertainties, defined as the mean and standard deviation of the posterior distribution at each point, respectively. Finally, in Section 5 we describe the resulting model and discuss it.

2 DATA PROCESSING

2.1 Correction of sensor misorientation

Measurements of RFs and surface wave polarization require the rotation of the two horizontal components, but seismometer misorientation may bias the results. We estimate the component azimuths for each NECESS Array station by analysing the particle motions of teleseismic *P* waves using the method of Niu & Li (2011). We collect earthquakes with magnitudes greater than 5.5 in the epicentral distance range from 30° to 90° with signal-to-noise ratios (SNRs) larger than 5. For each station, we compare the backazimuth of each event with the horizontal projection of the *P*-wave polarization direction to estimate the misorientation. We average all estimates from earthquakes with consistent results and find that the average misorientation is small, meaning that there is little bias in the orientations, on average. However, there are six stations with misorientation azimuths $\geq 10°$, as summarized in Table 1. We correct the orientations for these six stations before we measure the Rayleigh wave H/V ratio and compute the RFs. In addition, seven other stations show instability of orientations over time and are also summarized in Table 1. These seven unstable stations are discarded. We do not correct misorientations less than 10° because below this level they may be caused by near station structures and will not affect our results significantly (Niu & Li 2011). The standard deviation of the misorientations after we correct the six stations and discard the other seven stations is 3.3° and the mean misorientation is −0.1°.

2.2 Rayleigh wave ellipticity (H/V ratio)

We use earthquakes with $M_w \geq 5.0$ (reviewed ISC bulletin) between September 2009 and March 2011, and from the NEIC PDE catalogue between March 2011 and August 2011, which yields a total of 3734 events. After correcting sensor misorientations (Section 2.1),

Table 1. Problematic stations.

Error type	Number of stations identified	Station name (orientation error detected)
Misorientation (constant error)[a]	6	NE56 (−12°), NE5A_1 (−15°), NE5C (178°), NE6F (175°), NE7F (−12°), NEAE (−10°)
Unstable orientation[b]	7	NE49, NE4B, NE61_2, NE7G, NE8I, NEAD, NE123
Unstable amplitude response[c]	6	NE3A, NE52, NE4B, NE7D, NE7G, NE9D

[a]Misorientation azimuths measured clockwise from the geographic north direction (as shown in brackets).
[b]At these erroneous stations, orientation estimates are not stable during the entire deployment time.
[c]Stations that have abnormal amplitude responses during some time identified by the H/V measurements.

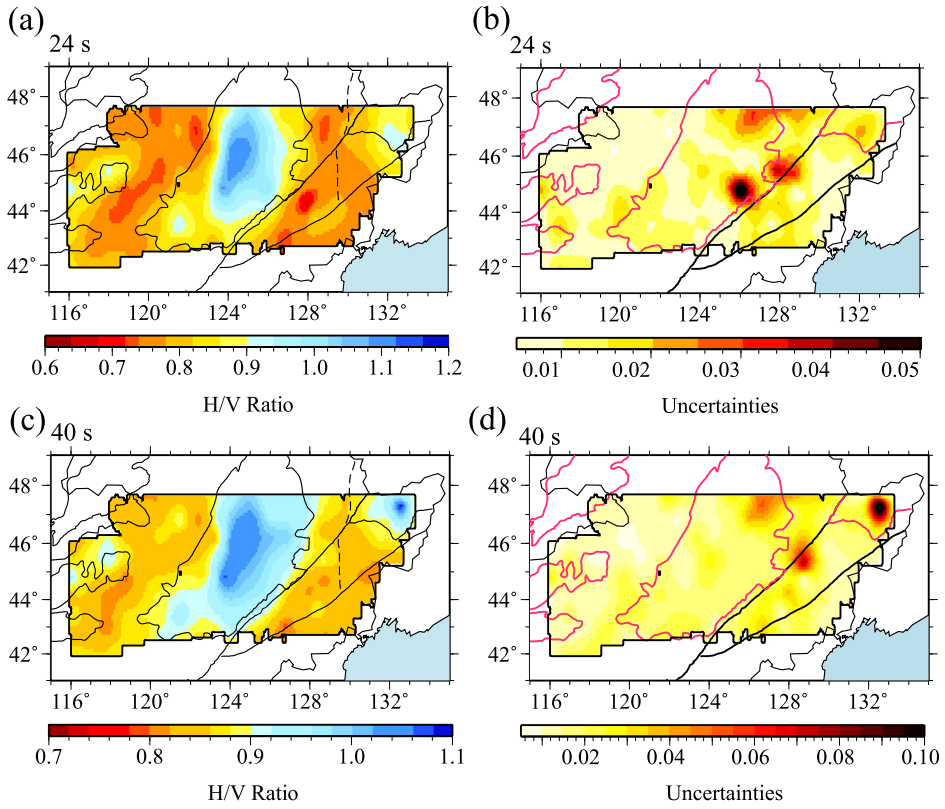

Figure 2. Example maps of Rayleigh wave H/V ratio (or ellipticity) at (a) 24 s and (c) 40 s period. Associated uncertainties in H/V ratio are also presented in (b) and (d).

we rotate the seismograms to get the radial and transverse components. For each earthquake, we apply automated frequency–time analysis (FTAN) at each station (Bensen *et al.* 2007) to measure the Rayleigh wave amplitudes on both vertical and radial components as well as the group and phase traveltimes. The H/V ratio measurements (the amplitude ratio of the radial and vertical components) are then obtained at periods between 20 and 80 s.

For each station and each period T, we follow Lin *et al.* (2012) to measure H/V but impose more strict criteria based on the data quality to ensure the reliability of the measurements. (1) We only keep those measurements with SNR larger than 15 on both radial and vertical components. (2) We require that the phase and group traveltimes measured on the radial and vertical components are consistent (i.e. $|tt_{ph\_R} - tt_{ph\_Z} - T/4| \leq T/8$ and $|tt_{gr\_R} - tt_{gr\_Z}| \leq 10$ s, where tt_{ph_R} and tt_{ph_Z} are phase traveltimes on the radial and vertical components, and tt_{gr_R} and tt_{gr_Z} refer to the group traveltimes). (3) We set the upper limit value of H/V to be 5. (4) We then take the average of all measurements from different earthquakes, remove 2σ outliers, and repeat this step once. If more than 20 measurements pass the above criteria, we use the mean and the standard deviation of the mean of these measurements as the H/V ratio and its uncertainty at each period. There are, for example, on average ∼180 earthquakes that pass the above criteria at 24 s period and ∼90 earthquakes at 40 s period. The uncertainty is somewhat underdetermined because systematic biases (e.g. azimuthal anisotropy) are not taken into account completely in our uncertainty estimation (Lin *et al.* 2014). Similar to our phase velocity measurements (see Section 2.3.1), we scale them up by a factor of 2 to compensate.

We identify six stations that have abnormal amplitude responses based on the H/V measurements. For each period, the H/V measurements at each station should be stable over time. However, for station NE3A, we observe that the measured H/V ratio increases by a factor of two during its deployment. This may be caused by the loss of the differential output of the vertical component of the seismograph. At station NE52, the H/V ratio is too low compared to nearby stations. At the other four stations, the H/V ratio measurements from a group of earthquakes that occurred in March 2011 show inconsistent high values. The reason for this problem is unknown and requires further investigation. We discard the measurements during suspicious abnormal time periods at these stations for both the H/V ratio and the following RF analysis (see Section 2.4).

The H/V ratio is particularly sensitive to the V_s structure in the upper few kilometres even at long periods (Lin *et al.* 2012). The estimated H/V ratio at 24 and 40 s period are shown in Fig. 2. The observed H/V ratios show clear correlations with geological features. High H/V ratios are observed in sedimentary basins (e.g. the Songliao, Erlian and Sanjiang basins) and low H/V ratios in mountain ranges (e.g. the GXAR, the ZGCR and the CBM). For the SLB, the central basin area and the Kailu depression in the southwest possessing relatively thick sedimentary fill are also clearly delineated by high H/V ratios. The estimated H/V ratio uncertainties at 24 and 40 s are generally smaller than 3 per cent of the estimated value, which is comparable to that measured beneath the USArray (Lin *et al.* 2014).

Examples of estimated H/V curves for stations NE53 and NE8C are shown in Figs 3(c) and (d). Station NE53 lies in the GXAR west of the SLB and station NE8C lies in the SLB (Fig. 1b). The curves are quite different. The higher values at NE8C are characteristic of sedimentary basins.

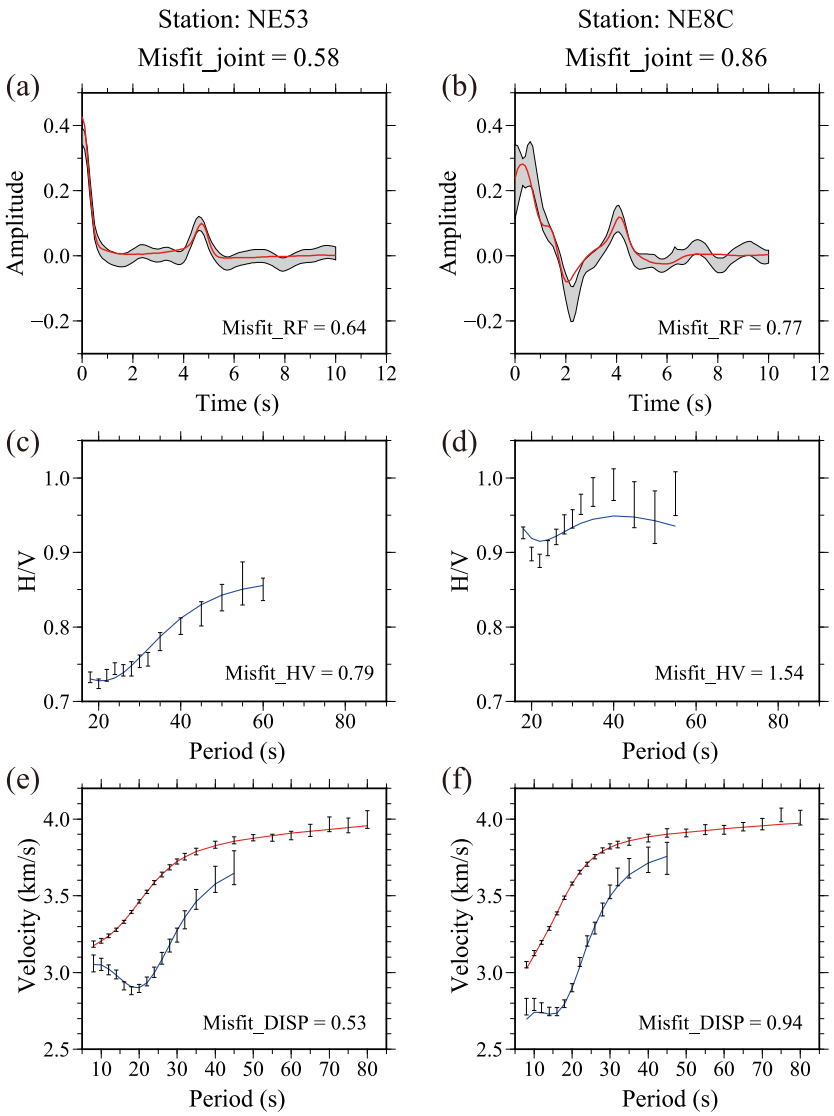

Figure 3. Examples of data used in the joint inversion for stations (Left Column) NE53 and (Right Column) NE8C, whose locations are identified in Fig. 1(b). (a,b) Receiver functions with uncertainties shown as the grey envelopes, (c,d) Rayleigh wave H/V ratios where uncertainties are presented as one standard deviation error bars and (e,f) Rayleigh wave group and phase speed curves with uncertainties presented as one standard deviation error bars. Solid lines in each panel are the predictions from the mean of the posterior distribution of model beneath each station, where for dispersion the red line is phase speed and the blue line is group speed. RMS misfit for the mean of the posterior distribution is presented for each data type alone on each panel and for the joint inversion at top of each column.

2.3 Rayleigh wave dispersion

2.3.1 Earthquake tomography

We apply Helmholtz tomography (Lin & Ritzwoller 2011) to Rayleigh wave measurements from the earthquake data set discussed in Section 2.2 (compiled for H/V measurements) to determine Rayleigh wave phase velocity maps from 30 to 80 s period on a $0.2^\circ \times 0.2^\circ$ grid. For each earthquake and wave period, FTAN is applied to measure the Rayleigh wave amplitudes and phase traveltimes on the vertical component at each station. Phase velocities at each location are then determined locally by calculating the gradient of the traveltime field and the Laplacian of the amplitude field (the finite frequency correction term). We discard all measurements with Rayleigh wave SNR less than 8. Following Lin & Ritzwoller (2011), the 2π phase ambiguity is resolved and measurements from particular earthquakes are discarded following criteria based on the curvature of the phase traveltime and amplitude surfaces across the array. We only obtain results at locations where there are measurements from more than 50 earthquakes. On average, measurements from about 350 earthquakes are used at each location at 30 s period and 110 earthquakes at 70 s period. We then calculate the mean and the standard deviation of the mean over all measurements from different earthquakes to estimate the isotropic phase velocity and its uncertainty at each location.

In contrast with eikonal tomography, Helmholtz tomography takes into account the finite frequency effect by introducing an amplitude dependent correction term, which tends to reduce both random as well as systematic errors (Lin & Ritzwoller 2011). We find that the average uncertainties for the isotropic phase velocity maps after the finite frequency correction are reduced. A comparison of the isotropic phase velocity maps with (Helmholtz tomography) and without (eikonal tomography) the finite frequency correction at 60 s period is shown in Fig. 4. The standard deviation of the

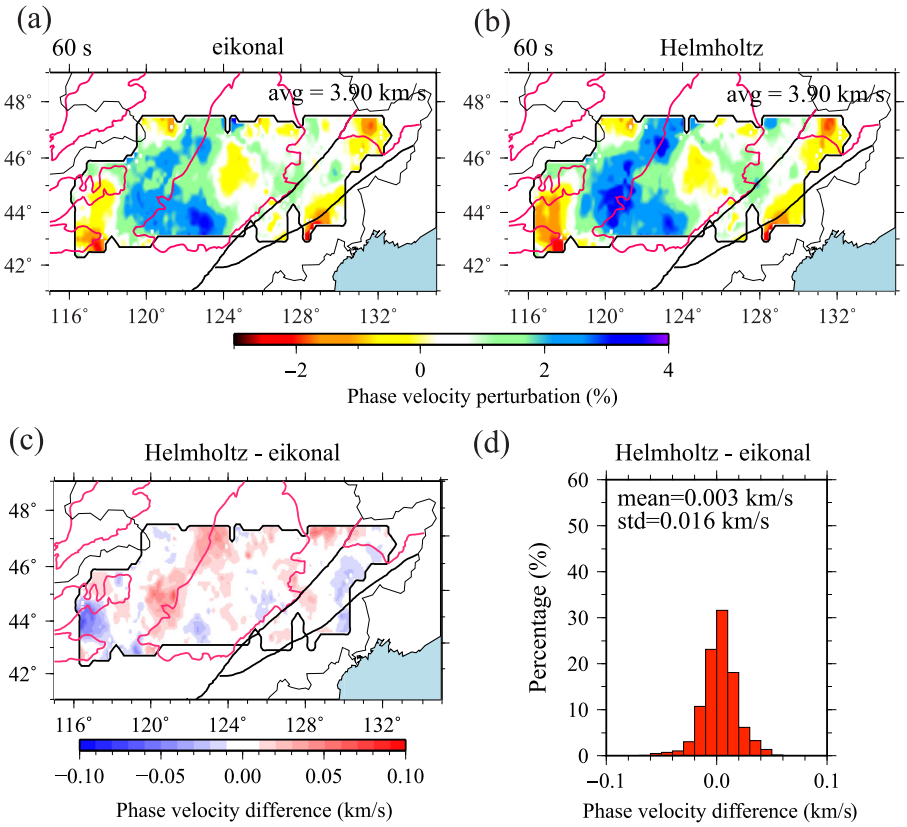

Figure 4. Comparison between earthquake-based tomographic maps for the 60 s Rayleigh wave using (a) eikonal tomography and (b) Helmholtz tomography. (c) The difference between the two maps. (d) Histogram of the differences between the two maps: mean difference is 3 m s^{-1}, standard deviation of the difference is 16 m s^{-1}.

differences between the isotropic phase velocity maps from Helmholtz and eikonal tomography is 7 m s^{-1} at 40 s and 16 m s^{-1} at 60 s period, consistent with the expectation that the magnitude of the finite frequency correction increases with period.

Raw uncertainty estimates in Helmholtz/eikonal tomography are usually underestimated (e.g. Lin *et al.* 2009) for two reasons: individual measurements at particular locations and periods are not entirely independent (Shen *et al.* 2015). Following Xie *et al.* (2015) and Lin *et al.* (2009), the uncertainties in the isotropic maps are scaled up (by a factor of 2 in this study) to encompass the differences between the ambient noise and earthquake tomography maps. Shen *et al.* (2015) describe and document this process in detail, and assimilate the measurements we obtain in their study. These measurements, therefore, have been included in the reference model China_2015.

2.3.2 *Ambient noise tomography*

We assimilate group and phase velocity measurements from ambient noise tomography (from 8 to 50 s period) from the earlier study of Shen *et al.* (2015). These data are the basis for the reference model China_2015. This study applied the straight ray tomography method of Barmin *et al.* (2001) to produce isotropic Rayleigh wave group and phase velocity maps on a 0.5° × 0.5° grid that extends well outside our study area. Examples of Rayleigh wave phase velocity maps are presented in Fig. 5 at periods of 10, 20, 30 and 40 s from ambient noise tomography as well as at 40 s from earthquake tomography. The ambient noise maps extend throughout China. Azimuthal anisotropy was estimated simultaneously to minimize anisotropic bias in the dispersion maps.

2.3.3 *Construction of group and phase velocity curves at each station*

We produce Rayleigh wave group and phase velocity maps every 2-s-period from 8 to 32 s and then every 5-s-period from 35 to up to 80 s. For the ambient noise map, we only keep the measurements at those locations where the resolution is better than 160 km. Uncertainties in the ambient noise and earthquake derived maps are discussed by Shen *et al.* (2015). We merge the ambient noise and earthquake tomography maps together with their uncertainties and generate maps on a 0.5° × 0.5° grid. At short periods (8–30 s), phase velocity maps are produced based on ambient noise alone; while at long periods (50–80 s) only earthquake tomography maps are used. In the period band of overlap (30–50 s), we average the phase velocity measurements and the uncertainties locally from the ambient noise and earthquake tomography maps, weighting up the ambient noise tomography maps at shorter periods and the earthquake based maps at longer periods. Examples of Rayleigh wave phase speed maps at 40 s period based on ambient noise and earthquake data are presented in Figs 5(d) and (e). Shen *et al.* (2015) argue that the differences between these maps, with a standard deviation of 27 m s^{-1}, are within the stated uncertainties. We then interpolate the phase velocities from a regular grid to each station location. Phase velocity curves at each station are constructed by averaging the velocities at the nearby grid points (distance <0.6°), taking the Gaussian function of the distance as the weight. The group velocity

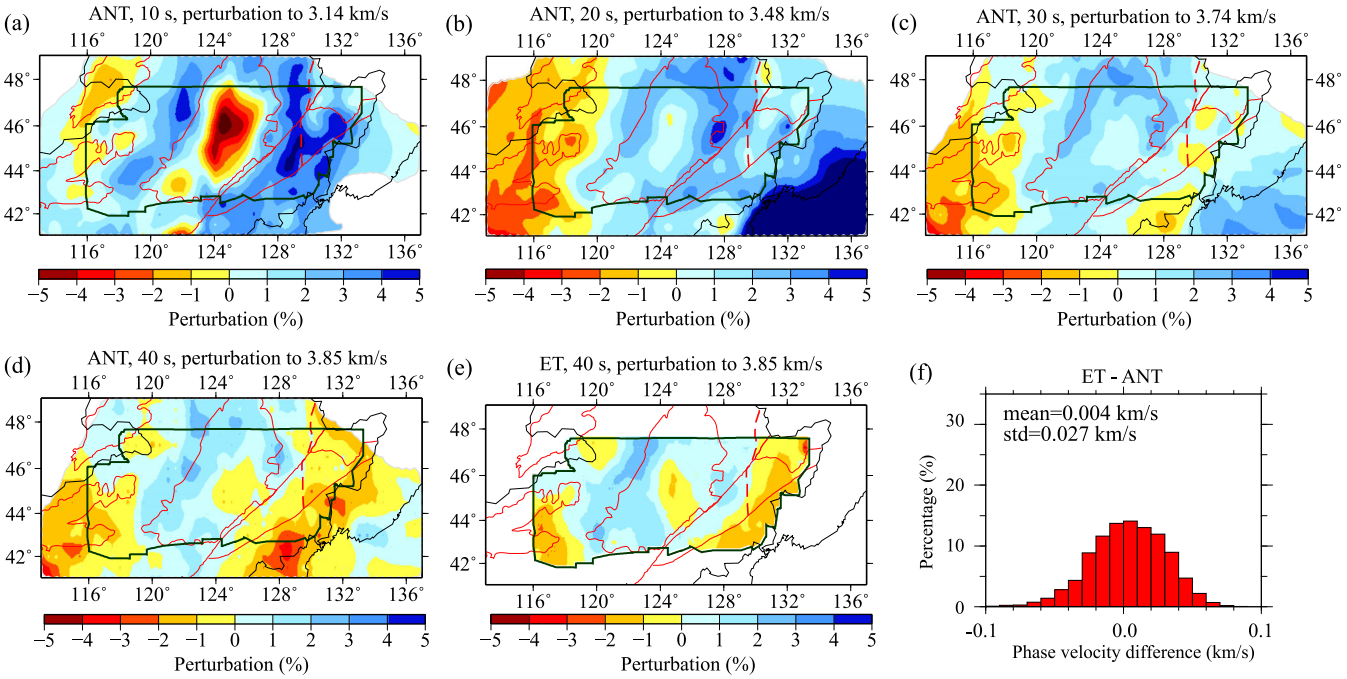

Figure 5. (a–d) Example Rayleigh wave phase speed maps determined from ambient noise tomography by Shen *et al.* (2015) at four periods: 10, 20, 30 and 40 s. (e) Rayleigh wave speed map determined by Helmholtz (earthquake) tomography at 40 s period to compare with the ambient noise result in (d). (e) Histogram of the difference between the 40 s maps from ambient noise and earthquake tomography: mean difference is 4 m s^{-1}, standard deviation of the difference is 27 m s^{-1}.

curves are derived only from the ambient noise maps and extend from 8 s to 50 s.

Figs 3(e) and (f) show examples of Rayleigh wave group and phase speed curves and uncertainties (presented as one standard deviation error bars) for two sample stations: NE53 and NE8C, whose locations are identified in Fig. 1(b). As with the Rayleigh wave H/V ratios at these stations, the dispersion curves at two stations differ appreciably; for example, group speed at short periods is much lower beneath the SLB.

2.4 RF data processing

We use teleseismic *P*-wave data from earthquakes with $M_w \geq 5.0$ and epicentral distances within 30°–95° from the centre of the array (total 1970 events) to produce radial component *P*-wave RFs. After the sensor misorientation correction (Section 2.1), we rotate the seismograms to get the radial and transverse components and apply the time-domain iterative deconvolution method (Ligorria & Ammon 1999), choosing a time window of [−20 s, 60 s] relative to the direct *P*-wave arrival time. This process utilizes an iterative linear inversion algorithm to perform the deconvolution in the time domain with an assumption that the resulting RF is a sum of Gaussian pulses. Under perfect circumstances, the convolution of the resulting RF with the vertical component will reproduce the radial component. However, the assumptions used in the deconvolution process prohibits the recovery to be perfect, and we can further use the recovery rate as a step of RF quality control, which will discussed in the next paragraph. A low-pass Gaussian filter with the width factor of 3 (pulse width ∼1 s) is used to suppress high-frequency noise in the RFs. Move-out corrections of both the time and amplitude of RFs are made to a reference slowness of 0.06 s km^{-1} based on the *Ps* phase generated from the *P*-to-*S* conversions off Moho.

Following Shen *et al.* (2013a), we impose several selection criteria. (1) Based on the analysis of Section 2.1, the estimated component azimuths from analysing the particle motions of teleseismic *P*-waves should be stable over time. We find, however, that 30 stations show inconsistency in the estimated component azimuths during some time periods, among which seven are identified as erroneous stations with possible instrument errors because the estimated component azimuths scatter during the entire deployment time. This may result from abnormal instrument responses. We discard the RFs during such suspicious abnormal times before further analysis. Note that the criteria we impose on the H/V ratio measurements already have largely eliminated the measurements during the suspicious abnormal times, so we do not apply this additional quality control to H/V ratio measurements, except for rejection of these seven erroneous stations. (2) As discussed in Section 2.2, we also discard the RFs during suspicious abnormal time periods recognized by the H/V ratio analysis. (3) We discard RFs whose product with the vertical component seismogram poorly approximates the radial component (<80 per cent recovery rate of the observed power in the radial seismogram). (4) We delete RFs with abnormal values: the amplitude of RFs should be less than 1 and the value at zero time should be positive. (5) We further remove inconsistent RFs by comparing them with the RF averaged over back-azimuthal groups (the 2-norm distance should be less than 0.1). On average, about 160 RFs are selected for each station.

Shen *et al.* (2013a,b) proposed the 'harmonic stripping' method in which raw single-event RFs that pass quality control are fit by a truncated harmonic function $H(\theta,t)$ as follows:

$$H(\theta, t) = A_0(t) + A_1(t)\sin[\theta + \theta_1(t)] + A_2(t)\sin[2\theta + \theta_2(t)], \quad (1)$$

where $H(\theta,t)$ is called the estimated RF. The fitting is done to estimate the azimuthally independent component $A_0(t)$ which

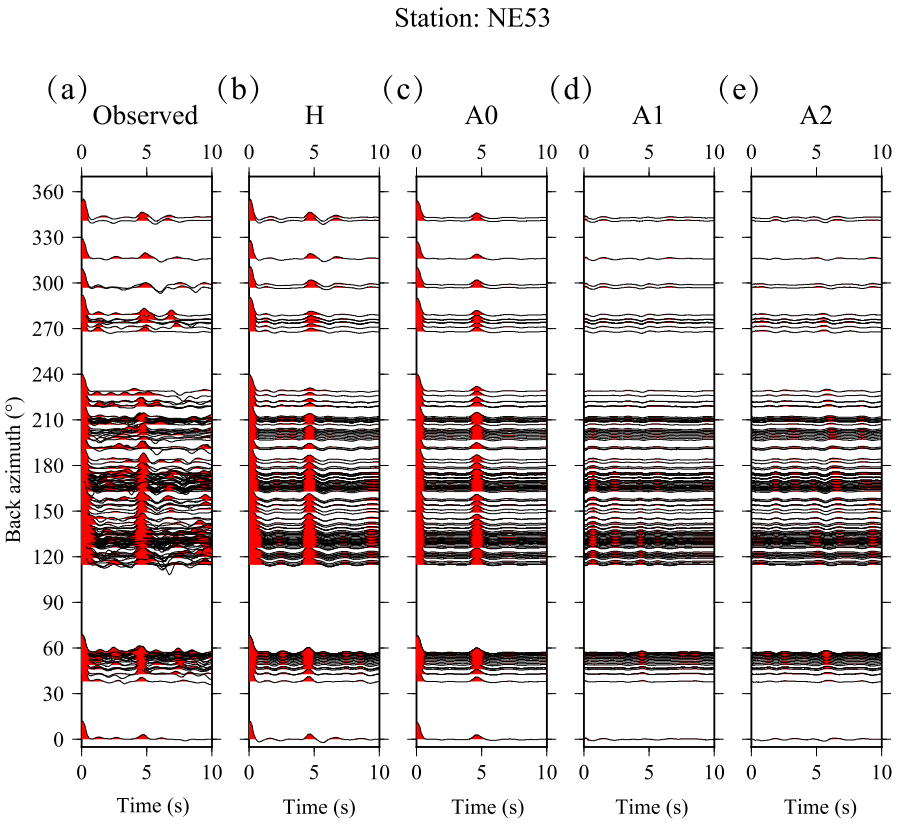

Figure 6. (a) The quality-controlled observed receiver functions are plotted along backazimuth for station NE53 (location identified in Fig. 1b). (b) The estimated receiver functions, $H(\theta,t)$, from harmonic stripping. (c–e) The three estimated harmonic components from harmonic stripping. For most stations, the receiver function we use in the joint inversion here is the average of $H(\theta,t)$ between azimuths of 120° and 240°.

represents the azimuthally isotropic average of the structure beneath the receiver. Examples of the raw RFs, the estimated RFs $H(\theta,t)$, and the harmonic component $A_0(t)$, $A_1(t)$ and $A_2(t)$, are presented in Fig. 6. This figure demonstrates an important characteristic of RF's in Northeast China; namely, that the vast majority of earthquakes lie in the azimuthal range from 120° to 240°, lying in the range from the southeast to the southwest of each station. (More than 75 per cent of the events are within this back-azimuth range.) When the back-azimuthal coverage of the RFs is sparse, $A_0(t)$ may not provide a good estimate of local azimuthally independent structure. For this reason, we modify the harmonic stripping method. Instead of using $A_0(t)$ as the azimuthally independent RF, we average $H(\theta,t)$ between 120° and 240° azimuth and find that this provides a more repeatable and reliable representation of local isotropic structure.

As an estimate of uncertainty, we compute the RMS difference between $H(\theta,t)$ and the observed RFs and use it as the 1σ uncertainty of the average estimated RF at each time. We believe that the uncertainties estimated in this way are somewhat overestimated (Shen *et al.* 2013a); therefore we scale them down by a factor of 2 to compensate. If uncertainties are unreasonably low (less than 0.02), we enlarge them to 0.02. We also double the uncertainties for nine stations if the number of raw RFs that pass the above criteria is less than 10 or the quality of RF is relatively low.

Finally, for stations showing particularly strong azimuthal variations, which we attribute to the effect of laterally varying structures, we choose an even narrower back-azimuthal range (120° to 180° or 180° to 240°) in which we average the RFs. This is performed at 13 stations. For these stations, the average RFs from different back-azimuthal groups show different features, which means that simply stacking them together will not represent average structure near the station. In this case we choose the back-azimuthal range where the RFs appear more representative of local structure and more in agreement with the parametrization we use to fit our model. For example, if RFs in an azimuthal subrange present evidence for a strong mid-crustal discontinuity we are likely to choose another range that does not present such evidence.

Example RFs are shown in Figs 3(a) and (b) for stations NE53 and NE8C. As with the dispersion data and the H/V measurements, they are quite different. The RF at station NE8C displays reverberations caused by sediments in the SLB which obscures the *Ps* converted phase at the Moho, while the RF at station NE53 in the GXAR displays a prominent converted phase. RFs such as the one shown in Fig. 3(b), which display strong reverberations due to sediments, are commonly viewed in RF studies as non-informative because they do not provide strong constraints on crustal thickness. However, in our joint inversion, such RFs are enormously useful because they provide strong constraints on sedimentary velocities and thickness.

3 JOINT INVERSION OF RAYLEIGH WAVE ELLIPTICITY (H/V), RAYLEIGH WAVE DISPERSION AND RFs

Surface wave phase and group speeds are sensitive to the averaged V_s velocities over depths based on their sensitivity kernels, which deepen with period, but weakly constrain discontinuity depths or velocity jumps across the discontinuities. Figs 7(a) and (b) present the depth sensitivity of Rayleigh wave group and phase velocity, respectively. At this period, group and phase velocity provide

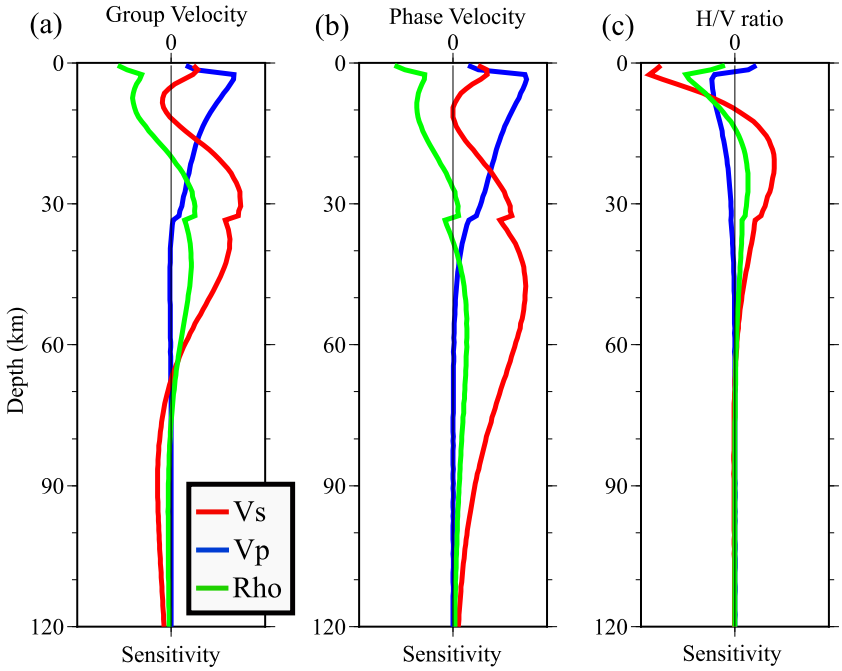

Figure 7. Depth sensitivity of 30 s Rayleigh wave group and phase velocities and H/V ratio. These sensitivities are computed based on the resulting average model at station NE53 presented in Fig. 9. (a) Depth sensitivity to V_s (red curve), V_p (blue curve) and density (green curve) for 30 s Rayleigh wave group velocity. (b) Same as (a), but for 30 s Rayleigh wave phase velocity. (c) Same as (a), but for 30 s Rayleigh wave H/V.

information at depths from about 30 to 60 km. RFs, in contrast, serve as a good complement to surface wave dispersion due to the information they provide about velocity contrasts. The joint inversion of surface wave dispersion and RFs has evolved to become a more effective means to resolve crustal and upper mantle structure than inversions based on either data set alone (e.g. Julià *et al.* 2000; Chang *et al.* 2004; Bodin *et al.* 2012; Shen *et al.* 2013a,b). Rayleigh wave ellipticity, or H/V (horizontal-to-vertical) ratio, is particularly sensitive to very shallow earth structure (e.g. Boore & Toksöz 1969; Tanimoto & Rivera 2008; Yano *et al.* 2009). Recently, Lin *et al.* (2012) demonstrated that intermediate to long-period H/V ratio measurements of earthquake surface wave signals are robust and compatible with traditional phase velocity measurements and can be used together with dispersion measurements to improve the resolution of crustal structures, especially in the several kilometres directly beneath the surface. Fig. 7(c) presents the depth sensitivity of the H/V ratio. In contrast with the sensitivity of phase/group velocities, the 30 s H/V ratio has its peak sensitivity at depths <5 km, and changes sign at greater depths. As a result, using H/V alone to infer the subsurface structure suffers strongly in velocity trade-offs. In this study, we apply a non-linear Bayesian Monte-Carlo algorithm (Shen *et al.* 2013a) to estimate V_s structure by jointly interpreting Rayleigh wave velocities, RFs and Rayleigh wave ellipticity data. To the best of our knowledge, this is the first study to use these three data sets simultaneously.

3.1 Model parametrization

Because Rayleigh waves are primarily sensitive to vertically polarized shear wave speeds (V_{sv}) rather than horizontally polarized shear wave speeds (V_{sh}), here we assume an isotropic V_{sv} model where $V_s = V_{sh} = V_{sv}$. RFs are used from 0–10 s and the longest period of surface waves that we use is 80 s, which provides reliable information about the top 150 km of the crust and uppermost mantle. We invert for a local 1-D model beneath each station rather than on a regular grid, and form the 3-D model by compiling the complete set of 1-D models. Following Shen *et al.* (2013a,b), we impose a smooth parametrization vertically between interfaces.

The 1-D model beneath each station is parametrized with three principal layers: a sedimentary layer with a linear velocity gradient with depth, a crystalline crustal layer, and a mantle layer. (1) The sedimentary layer is described by layer thickness and V_{sv} values at the top and bottom of the layer. (2) The crystalline crustal layer is described by six parameters: layer thickness and five B-splines for V_{sv}. (3) Mantle structure is modelled from the Moho to 200 km depth with five B-splines for V_{sv}. As seen in Fig. 7, both the Rayleigh wave dispersion and H/V are sensitive to V_p and density, but it is V_s to which they are most sensitive. As a result, in this study we are still solving for Vs primarily, but scaling V_p and density from V_s. We set the V_p/V_s ratio to 2.0 in the sedimentary layer and 1.79 in the mantle based on AK135 (Kennett *et al.* 1995) and use the scaling relation from Brocher (2005) in the crystalline crustal layer. For density, we use the relation based on Brocher (2005) in the crust and Hacker and Abers (2004) in the mantle. We apply a physical dispersion correction (Kanamori & Anderson 1977) using the Q-model from AK135 in the crust (Kennett *et al.* 1995) and the global model from Dalton & Ekstrom (2006) in the mantle. The smoothness of the model is imposed by the parametrization so that ad hoc damping is not needed during the inversion (Shen *et al.* 2013a,b).

We also find that for some stations located in the basins, we need to add one more unconsolidated sedimentary layer to fit the data, which is also supported by previous RF studies (Tao *et al.* 2014). For basin stations at which the resulting misfit can be improved by more than 20 per cent (i.e. at 10 stations), we apply another parametrization by adding a thin sedimentary layer with a linear velocity gradient with depth on the top and set the V_p/V_s ratio to 3.0 in this layer (Tao *et al.* 2014). Most of these locations are in the SLB, but some are in the Hailar, Erlian and Sanjiang basins. Stations

Table 2. Model parametrization.

Model parameters	Perturbation
Sedimentary layer thickness	±100 per cent
Sedimentary layer V_{sv}	±1.5 km s^{-1}
Crystalline crustal thickness	±15 km
B-spline coefficients, crust	±20 per cent
B-spline coefficients, mantle	±20 per cent

where there are one or two sedimentary layers are identified in Fig. 1(b).

3.2 Prior and posterior distributions

The model space for Monte Carlo sampling is defined relative to a starting model (Zheng *et al.* 2011) with perturbations defined in Table 2. For sedimentary basins, we enlarge the sedimentary thickness in the starting model based on previous geological cross sections (Wei *et al.* 2010; Zhang *et al.* 2012; Chen *et al.* 2014). Additional model constraints are imposed: (1) $V_s < 4.9$ km s^{-1} at all depths; (2) velocity increases monotonically with depth in the crystalline crust; (3) the velocity contrasts across the sedimentary basement and the Moho discontinuity are positive (Shen *et al*. 2013b). Examples of the prior distribution for particular model variables are presented in Fig. 8 as white histograms, and discussed further in Section 3.4.

Following the procedure described by Shen *et al.* (2013a,b), a random walk in the model space is performed guided by the Metropolis algorithm (Mosegaard & Tarantola 1995). Models are accepted if their misfit is less than 1.5 times that of the best fitting model. The posterior distribution of models is the ensemble of all accepted models and its statistical properties quantify model uncertainties. RMS misfit is the square root of the joint χ^2 misfit, which is defined as follows:

$$\begin{aligned}\sqrt{\chi^2_{\rm joint}} &= 0.5\cdot\sqrt{\chi^2_{\rm SW}} + 0.5\cdot\sqrt{\chi^2_{\rm RF}}\\ &= 0.5\cdot\sqrt{\frac{1}{N}\sum_{i=1}^{N}\frac{[g_i(m)-D_i^{\rm obs}]^2}{\sigma_i^2}}\\ &\quad + 0.5\cdot\sqrt{\frac{1}{L}\sum_{i=1}^{L}\frac{[R_i(m)-H(t_i)]^2}{\sigma_i^2}},\end{aligned}$$

where $g_i(m)$ is the predicted Rayleigh wave phase or group speed or H/V ratio, $D_i^{\rm obs}$ is the observed Rayleigh wave phase or group speed or H/V ratio; $R_i(m)$ is the predicted RF; $H(t_i)$ is the observed RF; σ_i is the corresponding one standard deviation uncertainty of the observation; N, L are the number of surface wave measurements (including the phase/group velocities and H/V ratio at different periods) or discrete times in the RF, respectively. Examples of posterior distributions are also presented in Fig. 8 as red histograms.

3.3 Fit to the data

Due to the various data acceptance and rejection issues described in Section 2, not all stations have data from the same measurements. The vast majority of stations, 105 in total, have all three data sets: surface wave dispersion, H/V and RFs. However, 12 stations have only Rayleigh wave dispersion measurements and RFs, 3 stations have dispersion and H/V ratio alone and 9 stations have only dispersion measurements (Fig. 1b). The RMS misfit of the mean model in the posterior distribution (named as the average accepted model) in the joint inversion is 0.93 on average. 99 per cent of the stations have RMS misfit less than 1.5. If $\chi^2_{joint} \sim 1$ then data uncertainties are appropriately estimated and the model generally possesses the right number of degrees of freedom (Shen *et al.* 2015).

Surface wave dispersion is fit quite well in the joint inversion. For 78 per cent of the stations, the RMS misfit of the surface wave dispersion data for the average accepted model is less than 1. The average RMS misfit at all stations is 0.84 for the dispersion data.

For two stations, the current parametrization cannot fit the RF data well, so we discard the RFs for these two stations. For the remaining RF data, the RMS misfit for the average accepted model is 1.0 on average. 88 per cent of the stations have RMS misfit less than 1.5. The remaining stations with relatively large RF misfit are located mainly in the sedimentary basins.

For six stations, the RMS misfit of H/V measurements is larger than 2.5, while the RF and surface wave dispersion can be fit well. The reason may be that the H/V ratio is also sensitive to the density and V_p of the shallow structure (Fig. 7). For these stations we use the joint inversion of RF and surface wave dispersion only. The RMS misfit of the H/V ratio data for the average accepted model is 1.1 on average. 79 per cent of the stations have RMS misfit less than 1.5. The misfit level is generally smaller than that in the USArray (Lin *et al.* 2012; Lin *et al.* 2014). As a result, we conclude that the current model parametrization adequately fits the data for most of the stations, but for a small number of stations further efforts are called for to investigate the density/V_p anomalies or other complexities needed to fit every piece of data

Data fit can be seen explicitly in Fig. 3 for RFs, H/V and Rayleigh wave group and phase speeds for two stations: NE53 and NE8C. In each case predicted data are presented along with the data as solid lines, demonstrating how data are fit, on average. An example of poor fit to the H/V ratio is seen for station NE8C in the SLB. All of the other data at these two stations are fit quite well.

3.4 Improvement in the 3-D model compared with the surface wave inversion

While surface wave dispersion data primarily constrain the velocity structure between interfaces (e.g. Shen *et al.* 2015), RFs are sensitive to velocity contrasts. The H/V ratio further constrains upper crustal structure and thus mitigates artefacts spreading into deeper velocity structures (Fig. 7; Lin *et al.* 2012).

The assimilation of the H/V ratio and the RF data has greatly improved accuracy of the estimate of the depths to discontinuities and *S*-wave speeds near them. Fig. 8 shows examples (at station NE53 in the GXAR) of prior and posterior distributions for several variables (sediment thickness, crustal thickness, V_s at 30 km depth in the crust, V_s at 80 km depth in the uppermost mantle) from the inversion based on surface wave dispersion alone (Figs 2a–d) and all the three data sets (Figs 2e–h). In each panel, the prior distribution is presented as the white histogram and the posterior distribution as the red histogram. The distributions of the depth of discontinuities (i.e. sediment thickness and crustal thickness) are broad in the surface wave dispersion inversion. In contrast, in the joint inversion, sedimentary and crustal thicknesses are much more tightly constrained. For station NE53, uncertainty in crustal thickness reduces from 4.97 km using surface wave dispersion data to 1.58 km in the joint inversion and the mean value reduces by approximately 2 km. In contrast, the effects of introducing RFs and H/V in the joint inversion are more subtle on V_s at 30 and 80 km. At 30 km depth there is narrowing of the posterior distribution with a reduction of the standard deviation from 50 to 30 m s^{-1}. This

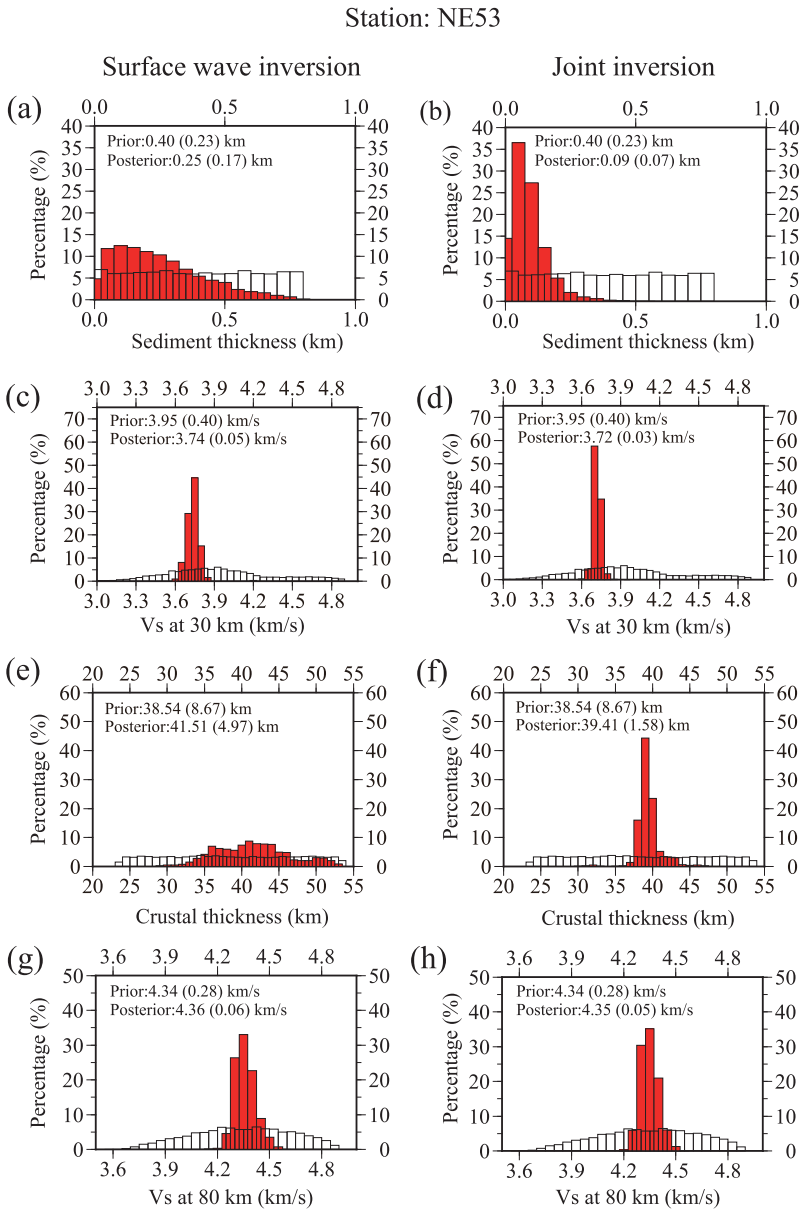

Figure 8. Examples of the prior and posterior distributions for several model variables at station NE53 (location identified in Fig. 1b), where the prior is shown with the white histogram and the posterior by the red histogram. The left column (a,c,e,g) is for the inversion based on surface wave dispersion alone and the right column (b,d,f,h) presents results from the joint inversion including receiver functions and H/V ratio. (a,b) Sedimentary thickness, in km. (c,d) V_s at 30 km depth in km s^{-1}. (e,f) Crustal thickness, in km. (g,h) V_s at 80 km, in km s^{-1}. The mean and standard deviation of both prior and posterior distributions are labelled on each panel, where the standard deviation appears in parentheses.

happens because the RFs ensure that this point lies in the middle crust, not in the lower crust or the mantle.

The posterior distribution is displayed in a different way in Fig. 9 for the joint inversion at two stations: NE53 and NE8C. In the depth functions, the grey profiles present the full width of the posterior distribution at each depth whereas the red lines show the one standard deviation profiles. The models beneath these two points, the former in the GXAR and the latter in the SLB, are quite different from each other. The station in the SLB has about 2 km of sediments and a mean crustal thickness of about 32.6 km whereas the crust is much thicker beneath the GXAR: 39.5 km.

The contrast between the average velocity structure of the shallow crust (top 4 km, including sediments) based on surface wave data alone and in the joint inversion is shown in Figs 10(a) and (c). In the joint inversion, the structures imaged are sharper laterally and the low velocity anomaly in the centre of the SLB is slower. Low velocities associated with the Erlian and Sanjian basins also appear. Perhaps more significantly, however, uncertainties are reduced strongly in the joint inversion as a comparison between Figs 10(b) and (d) illustrates. The V_s uncertainties for the uppermost crust are large when using surface wave dispersion alone (~0.17 km s^{-1} on average), especially beneath sedimentary basins, and reduce to ~0.11 km s^{-1} in the joint inversion.

Crustal thicknesses from the joint inversion (Fig. 10e) are also sharper and the variations are more tightly confined between geological boundaries than in the inversion from surface wave dispersion alone (Fig. 10g). Notably, very thin crust is found to rim the eastern edge of the SLB and thicker crust is confined within the Jiamusi

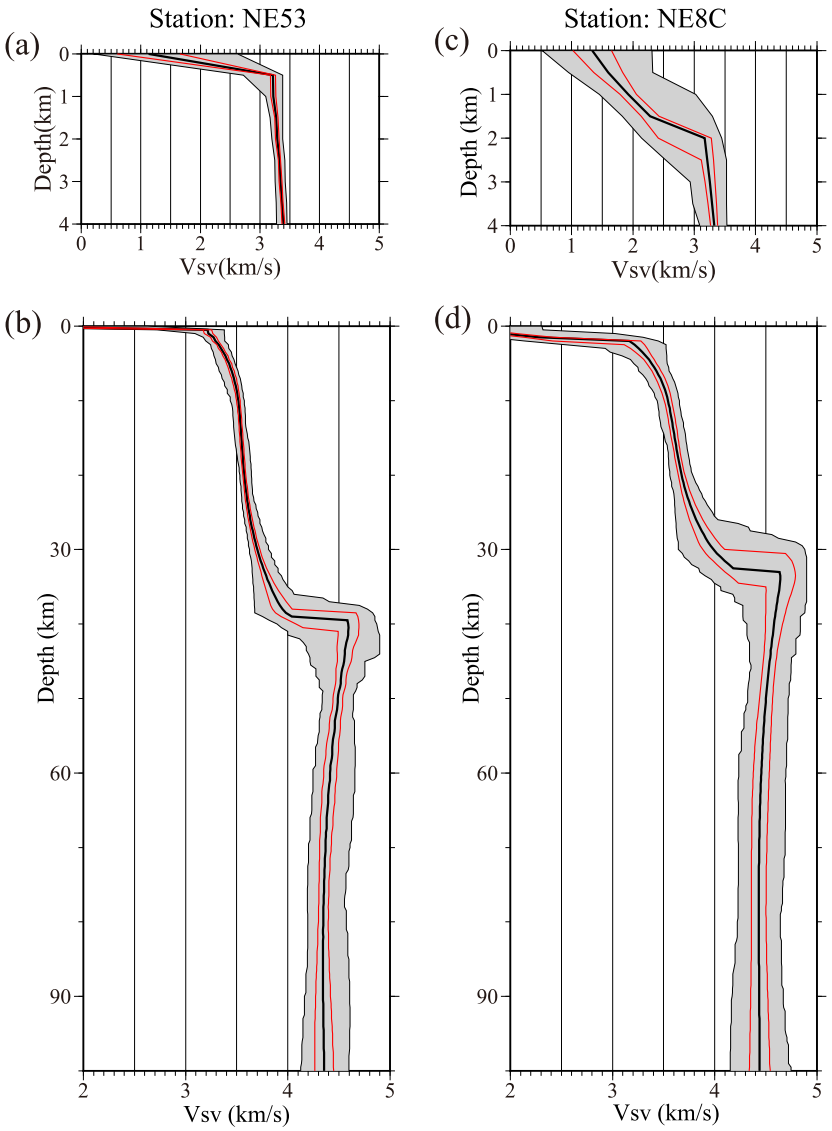

Figure 9. Vertical envelopes (grey shaded regions) formed by the full set of accepted models in the posterior distribution at two stations (NE53, NE8C) whose locations are identified in Fig. 1(b). The bold black lines identify the mean of each distribution (from which the solid curves in Fig. 3 are computed) and the red lines identify the one standard deviation perturbations in the posterior distribution at each depth.

Massif east of the Jiayin-Mudanjiang Suture. The crust is also found to be somewhat thinner beneath the GXAR in the joint inversion. Uncertainties in crustal thickness average about 2.8 km in the joint inversion compared to about 4.4 km in the inversion of surface wave dispersion alone. Regions of continued high uncertainty in crustal thickness in the joint inversion include parts of the SLB, where the Moho *Ps* signals are obscured by sedimentary reverberations, and the Jiamusi Massif and near the CBM, where there is a weak Moho *Ps* signal which we interpret as a gradient Moho caused perhaps by Moho complexity.

4 RESULTS AND DISCUSSION

After inversion is performed at all stations, we interpolate the V_s models onto a $0.5^\circ \times 0.5^\circ$ regular grid using simple kriging interpolation (Schultz *et al.* 1998) at each depth guided by the estimated uncertainties. Map views of the 3-D model are presented in Figs 10a,e and 11, and the uncertainties are presented in Figs 11b,f and 12.

4.1 Description and discussion of the 3-D model

For the uppermost crust, a clear correlation is observed between V_s structure and near surface geological features (Fig. 10a). Basin areas, such as the Songliao, Erlian and Sanjiang basins, are clearly delineated by low V_s anomalies. The slowest V_s anomalies of $\sim$2 km s^{-1} are observed in the northern SLB, nearer to its western margin than the eastern margin. This is consistent with the evolution of the basin in the Cretaceous Period, in which the eastern SLB was uplifted such that its depocentres migrated westward (Wang *et al.* 2007; Feng *et al.* 2010). A low V_s anomaly of $\sim$2.5 km s^{-1} is also resolved in the Southwest SLB, which is related to the Kailu depression (Feng *et al.* 2010; Guo *et al.* 2015). Also, sediments are much thicker in the northern SLB in our model, which may be explained by larger post-rift subsidence of the northern SLB than the southern part (Feng *et al.* 2010; Wei *et al.* 2010).

Shear wave speeds in the middle and lower crust show similar patterns of spatial variation (Figs 11b and c). Clear low V_s anomalies in the middle-to-lower crust are mainly observed beneath the GXAR (especially the southern and northern parts), the eastern margin

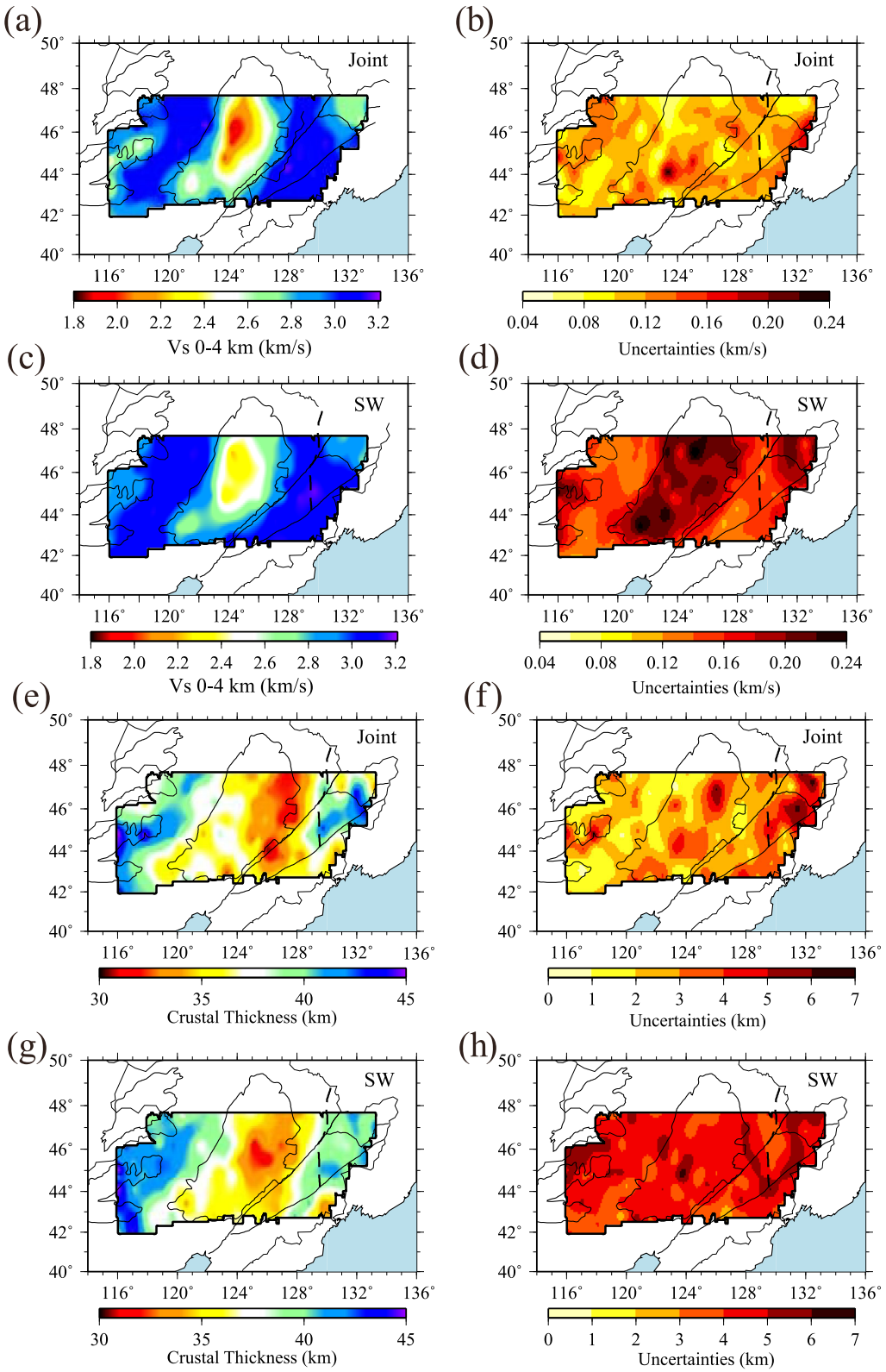

Figure 10. Comparison between the estimated models and uncertainties from the inversion of surface wave dispersion alone (SW) and from the joint inversion (surface wave dispersion, receiver functions and H/V ratio, Joint). Maps of the mean of the posterior distribution of the average of V_s at depths from 0 to 4 km from (a) the joint inversion and (c) the surface wave dispersion. Uncertainties in the V_s averaged from 0 to 4 km are shown in (b) and (d), where uncertainty is one standard deviation from the mean of the posterior distribution. (e,g) Mean of the posterior distribution of crustal thickness from the joint and surface wave inversions, respectively. (f,h) Associated one standard deviation uncertainties in crustal thickness.

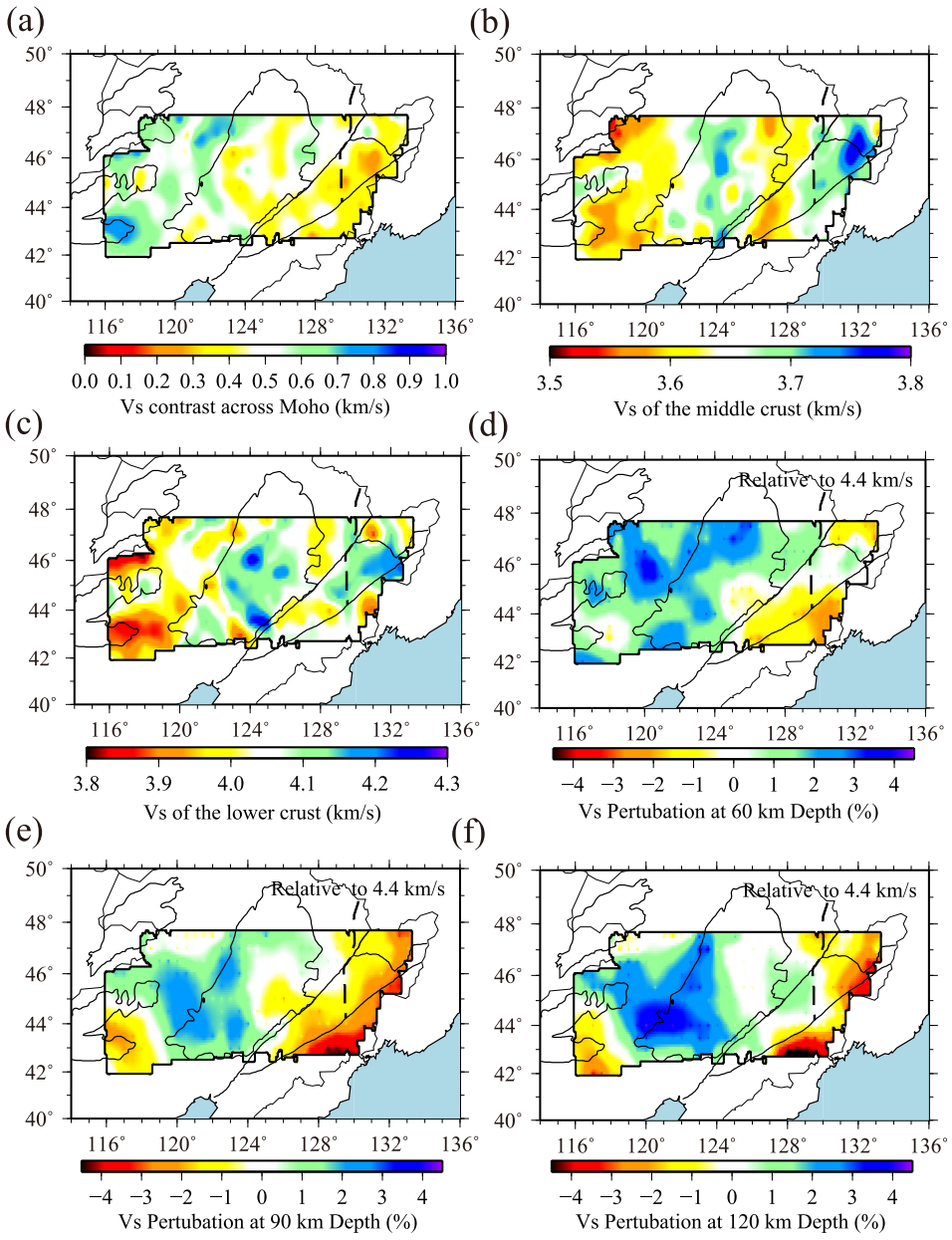

Figure 11. Maps of the mean of the posterior distribution at each location from the joint inversion for (a) the jump in V_s across the Moho (constrained to be positive), (b) V_s in the middle crust (averaged between ±2 km of the middle of the crystalline crust), (c) V_s in the lower crust (averaged from 4 km above Moho to Moho), (d) V_s at 60 km depth (averaged from 55 to 65 km), (e) V_s at 90 km depth (averaged from 80 to 100 km) and (f) V_s at 120 km depth (average from 110 to 130 km). Mantle velocities are defined as perturbations relative to 4.4 km s^{-1} (in per cent) and crustal velocities are plotted in absolute terms, km s^{-1}.

of the SLB and in the wedge formed by the Yilan-Yitong and Dunhua-Mishan faults west of the Jiayin-Mudanjiang Suture. The slow anomalies beneath the GXAR are adjacent to the locations of two Pleistocene volcano groups marked in Fig. 1(a), which we refer to as the North/South GXAR Pleistocene Volcanic Zones. Slow anomalies beneath the eastern margin of the SLB extend southward toward the western CBM are located in a region we refer to as the Northeast China Lineated Quaternary Volcanic Zone (Fig. 1a). The slow mid-crustal velocities beneath the GXAR are in accordance with granitic intrusions during the Mesozoic Era there (Wu *et al.* 2003a,b). Beneath the SLB the high V_s anomalies (which appear more prominently in the lower than middle crust) may reflect a more mafic composition associated with rifting during basin formation in the late Mesozoic (Zhang *et al.* 2011). The fast anomaly observed beneath the Jiamusi Massif, bounded by the Jiayin-Mudanjiang suture to the west, may either indicate old basement which has been transported to its current location by block tectonic processes or perhaps magmatic underplating. Alternately, this fast anomaly could represent contamination of crustal velocity estimates with mantle velocities because crustal thickness is not well determined in this area (Fig. 10f).

Crustal thickness varies strongly across the region of study, thinning from ∼45 km in the GXAR to ∼30 km beneath the eastern SLB in the centre of our study area (Fig. 10e). The most prominent anomaly is that Moho is uplifted about 6 km from west to east within the SLB, which agrees in general with estimates by Tao *et al.* (2014). The thinnest crust near the eastern margin of the SLB lies within the Northeast China Lineated Quaternary Volcanic

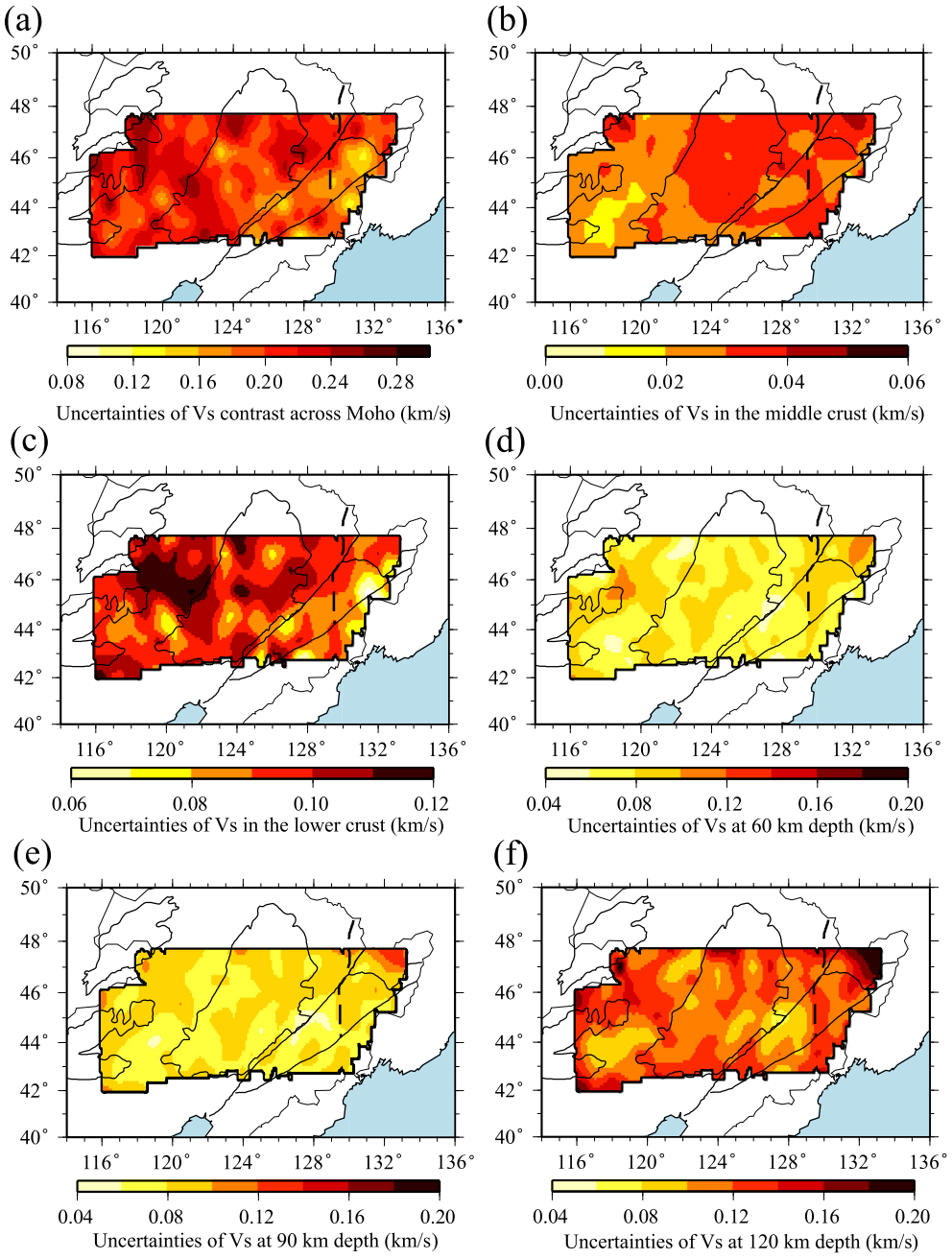

Figure 12. Maps of one standard deviation relative to the mean of the posterior distribution from the joint inversion, interpreted as local uncertainty, where the means of the corresponding variables have been plotted in Fig. 11.

Zone. Several hypotheses could explain the eastward thinning of the crust in the SLB. First, the crust may have been thinned by stretching, and volcanoes penetrated the region opportunistically. Alternately, the thinner crust may have been created actively by long standing episodic volcanism that initiated in the Cenozoic and migrated flankward (Liu *et al.* 2001; Chen *et al.* 2007; Tao *et al.* 2014). Or, topography on the Moho could be interpreted as a westward tilt caused by a change in the direction of Pacific subduction toward the west in the late Cretaceous (Stepashko 2006; Feng *et al.* 2010).

Relatively thick crust of ∼40 km is observed beneath the Jiamusi Massif near the eastward end of our study region which is in accordance with its long cooling history (Wu *et al.* 2011). However, the crustal thickness uncertainties beneath the Jiamusi Massif are large (Fig. 10f) because RF data show weak or complicated Moho *Ps* signals in this area. The V_s jump (Fig. 11a) across the Moho (∼0.6 km s^{-1}) is large beneath the GXAR and reduces somewhat beneath the SLB.

Across most of the study area we observe a thin 'lid' right below the Moho with about 20 km thickness. This can be seen most clearly in the vertical transects presented in Figs 13–16. The lid is largely imposed by the RFs, which constrain the jump in V_s across the Moho. A possible explanation for it may be higher densities caused by metamorphism of the mafic lower crust.

The strongest low velocity anomalies in the uppermost mantle are observed near the most active volcano in the region,

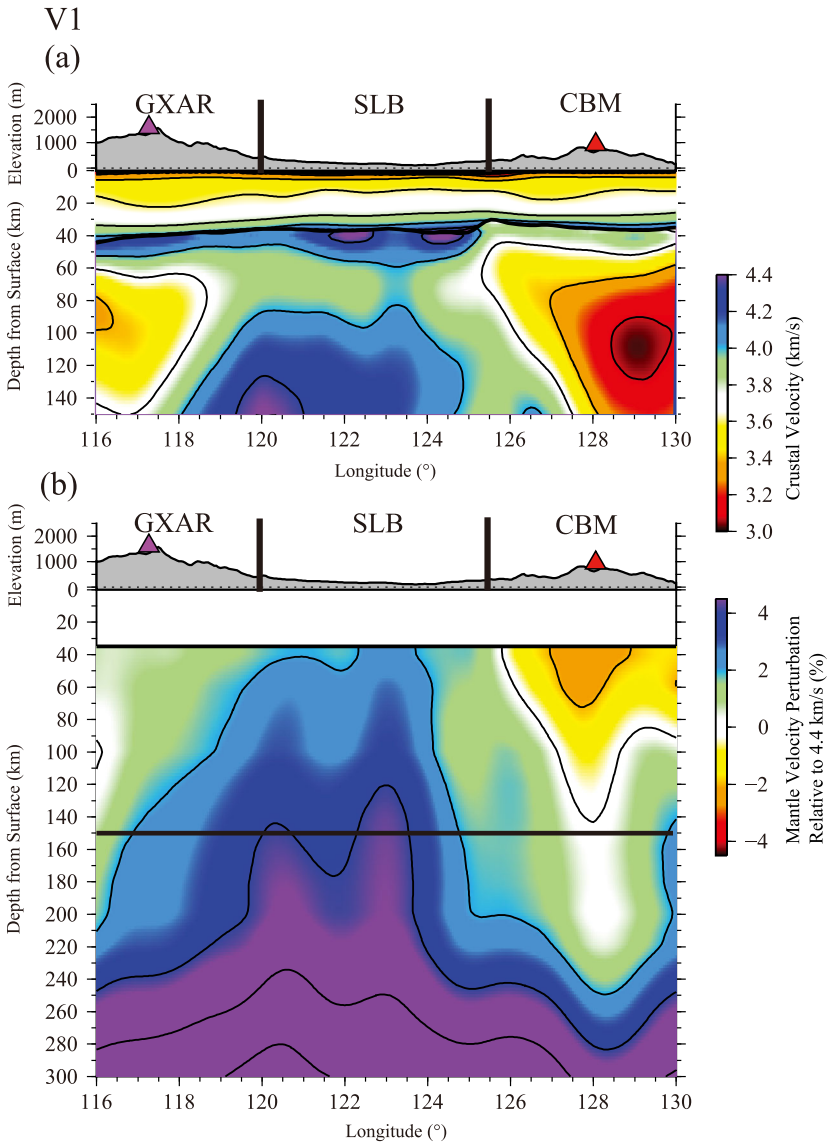

Figure 13. (a) A vertical transect (V1, location shown in Fig. 1b) through our V_S model plotted to 150 km, compared with (b) V_S values from the body wave model of Tang *et al.* (2014) plotted to 300 km depth. Absolute velocities are presented in the crust (in km s^{-1}) and in the mantle perturbations are plotted relative to 4.4 km s^{-1} (in per cent). Surface topography is indicated in each panel together with location names, defined in Fig. 1(a). Nearby volcanoes are also indicated, colour-coded by age as in Fig. 1(a).

Changbaishan Volcano, and generally east of the Yilan-Yitong Fault near the periphery of the study region (Figs 11d–f, and transects V1, V5 and V6, Figs 13 and 16). During the Cenozoic Era, including in the Holocene, volcanic eruptions in Northeast China migrated eastward to south of the Yilan-Yitong Fault (Liu *et al.* 2001; Chen *et al.* 2007). Vertical transects V1–V3, V4, and V5 all show this mantle low velocity anomaly east of the SLB. Lowest velocities are associated with the CBM and are best seen in transects V1, V5 and V6. Tang *et al.* (2014) interpret the low velocities found in the mantle beneath this part of our model as originating from subduction-induced upwelling that ascends through a gap in the subducting slab.

Lying beneath the thin slab extending below the SLB, there are low velocity anomalies shown in transects V1–V3 and V5. On average, the upper mantle beneath the eastern SLB is slower than the western SLB, as shown clearly by transects V2 and V3 in Figs 14 and 15, consistent with the model of Tang *et al.* (2014). This is presumably because of proximity to the Northeast China Lineated Quaternary Volcanic Zone, which is arrayed nearer to the eastern margin of the basin. The lowest velocity anomaly extends from about 60 to 100 km depth beneath the SLB, and appears strongest in transect V2. The vertically arrayed fast, slow, fast pattern of anomalies beneath the SLB requires further investigation, particularly addressing whether it may provide evidence for recent delamination or the onset of lithospheric instabilities in the region. Alternately, the feature may reflect the crystal preferred orientation of anisotropic mantle minerals causing radial anisotropy that we are unable to resolve due to the lack of Love wave measurements.

Slow anomalies in the mantle are also identified beneath the northern and southern GXAR (Figs 11d–f), which appear more clearly in the vertical transects V1 and V4 in Figs 13 and 16, respectively, near the locations of the Northern/Southern Greater Xing'an Range Pleistocene Volcanic Zones (Fig. 1a). In contrast, the central

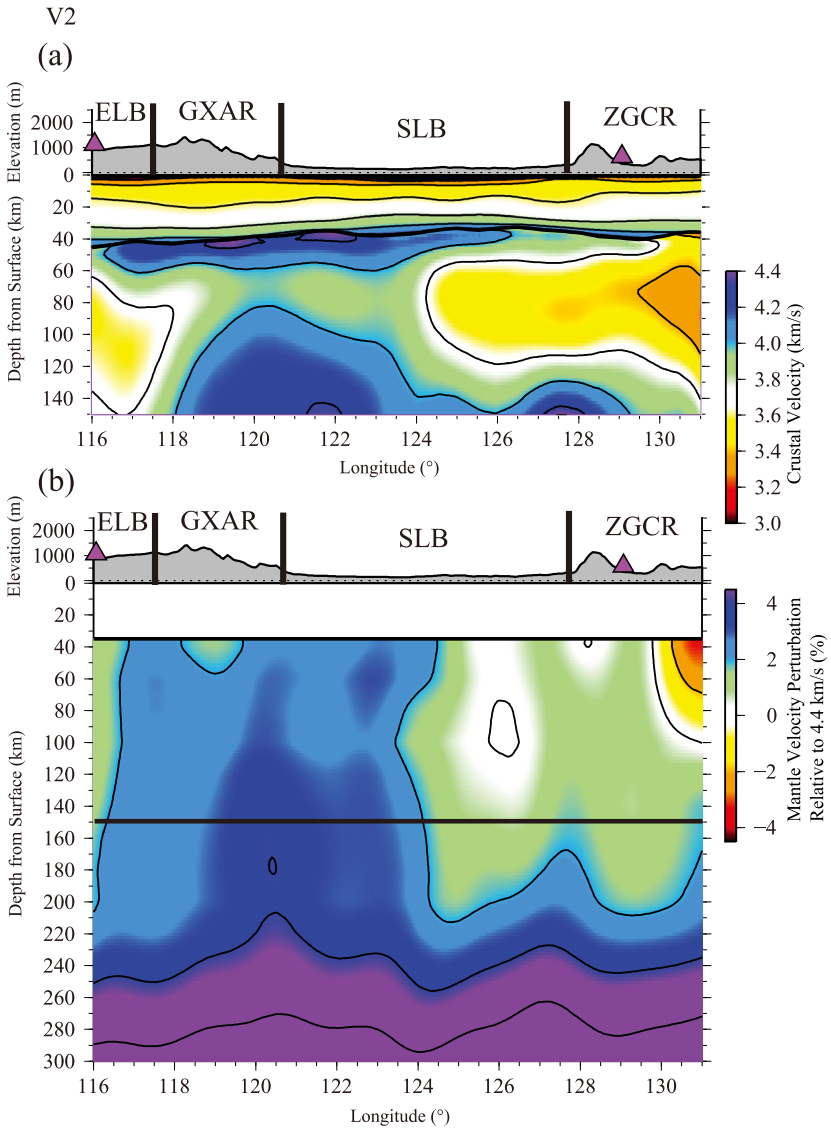

Figure 14. Similar to Fig. 13, but for vertical transect V2.

GXAR has high V_s anomalies in the upper mantle (transects V3 and V4) characteristic of thick lithosphere in this part of the mountain range. Thus, the mantle beneath the GXAR is inhomogeneous; only the northern and southern regions display mantle low velocities, which we interpret as thin lithosphere. The thin lithosphere beneath the southern and northern GXAR may be consistent with hypothesized previous episodes of delamination in the Mesozoic Era (Wang *et al.* 2006; Zhang *et al.* 2010) with later Cenozoic volcanism occurring only where thin lithosphere is present (Figs 1a and 16a).

4.2 Comparison of the 3-D model with previous studies

Our model is, in general, similar with those of Guo *et al.* (2015). Guo *et al.* (2015), used ambient noise data from NECESS stations and RF data from NECESS stations and seven CEA stations. They produced velocities from the surface to a depth of 60 km, while our study provides shear wave velocities to150 km depth, which are primarily constrained by long period surface waves from earthquake data. We find slow and fast anomalies of the middle and lower crust beneath the GXAR and the SLB, respectively, which are consistent with the results of Guo *et al.* (2015). Also, the uppermost mantle velocities in our model (Fig. 11d) show spatial variations similar to their results (fig. 5 in Guo *et al.* 2015). For example, strong low velocity anomalies beneath Changbaishan Volcano and east of Yilan-Yitong fault and weak low velocity anomalies beneath northern and southern GXAR are present in both models. However, there are several dissimilarities. Because we include H/V measurements, we are able to image very shallow structure in more detail and this accordingly influences the fine structure at greater depths. For example, the low velocity in the ELB and the SJB are more clearly resolved, and the SLB also shows finer scale features (Fig. 10a) compared with fig. 5 in Guo *et al.* (2015). Also, we resolve a low V_s feature beneath the GXAR and observe low velocity anomalies in the middle and lower crust along the eastern margin of the SLB. Finally, there are differences in the lower crust beneath the Jiamusi massif between the models. Some of these differences reflect different smoothing constraints, but are within model uncertainties (Figs 12b and c).

In addition, Tang *et al.* (2014) present a teleseismic *S*-wave tomography model across our study region, also based largely on data

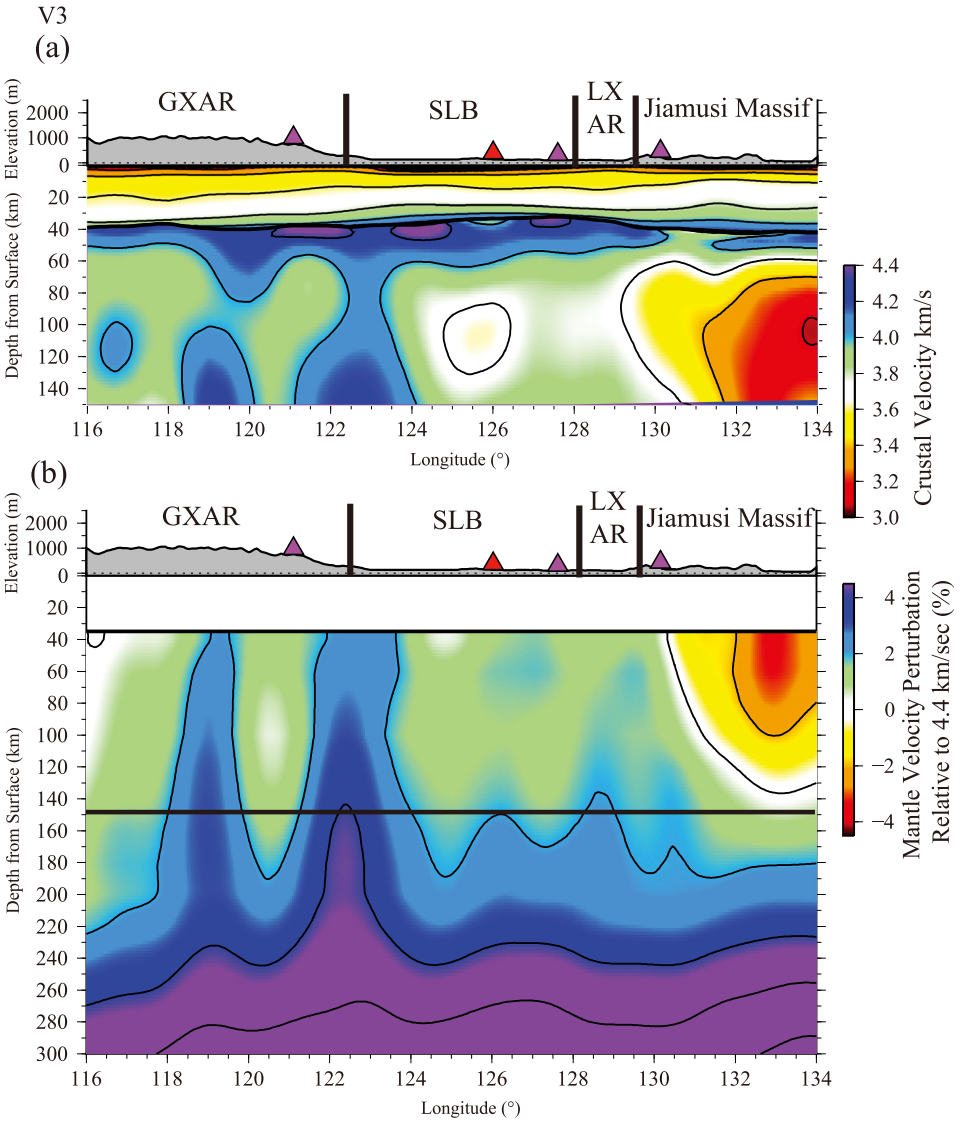

Figure 15. Similar to Fig. 13, but for vertical transect V3.

from the NECESS Array. Their model extends much deeper than ours and we present transects of this model to a depth of 300 km in Figs 13–15. We find that there are significant similarities between the two models in the lateral location of high and low velocities in the mantle, but there are dissimilarities concerning the distribution of the anomalies with depth. The lateral distribution of V_s anomalies, especially the outlines of sharp V_s contrasts display a high degree of consistency. A prominent high V_s anomaly, which bifurcates further north, is observed beneath the GXAR and the western flank of the SLB at depths greater than about 80 km in both models. In contrast, low V_s anomalies are shown near the CBM, the ZGCR and the Jiamusi massif. However, relatively weak low V_s anomalies beneath the southern GXAR, the ELB and the eastern flank of the SLB in our model are not clearly resolved in the body wave tomography. Moreover, the vertical distribution of V_s anomalies presents some discrepancies. For example, the slowest anomaly near the CBM is located at ∼110 km in our model, while it lies immediately below the Moho in Tang's model (Fig. 13). Perhaps the most notable difference between these two models is that a thin 'lid' at the top of the mantle is present in our model. The assimilation of RFs in our inversion reduces the trade-off between Moho depths with lower crustal velocity and helps to resolve this uppermost mantle structure (Shen *et al.* 2013a).

5 CONCLUSIONS

This study aims to refine the reference model China_2015 produced using surface wave dispersion data by Shen *et al.* (2015). We do this by assimilating the surface wave data in Northeast China used to construct China_2015 and introducing two new sets of measurements obtained using data from the NECESS array: RFs and Rayleigh wave H/V or ellipticity measurements. We document how the new data sets improve the vertical resolution of the resulting model within the crust, within the uppermost mantle, and between the crust and mantle and also improve the estimate of crustal thickness. Our 3-D model is produced on a 0.5° × 0.5° beneath the NECESS Array using a Bayesian Monte Carlo formalism in which the model and its uncertainties are determined from the mean and standard deviation of the posterior distribution of accepted models. A rich variety of structural features are revealed in the final model. The model we present agrees well in the lateral distribution of fast and slow anomalies in the mantle with the teleseismic

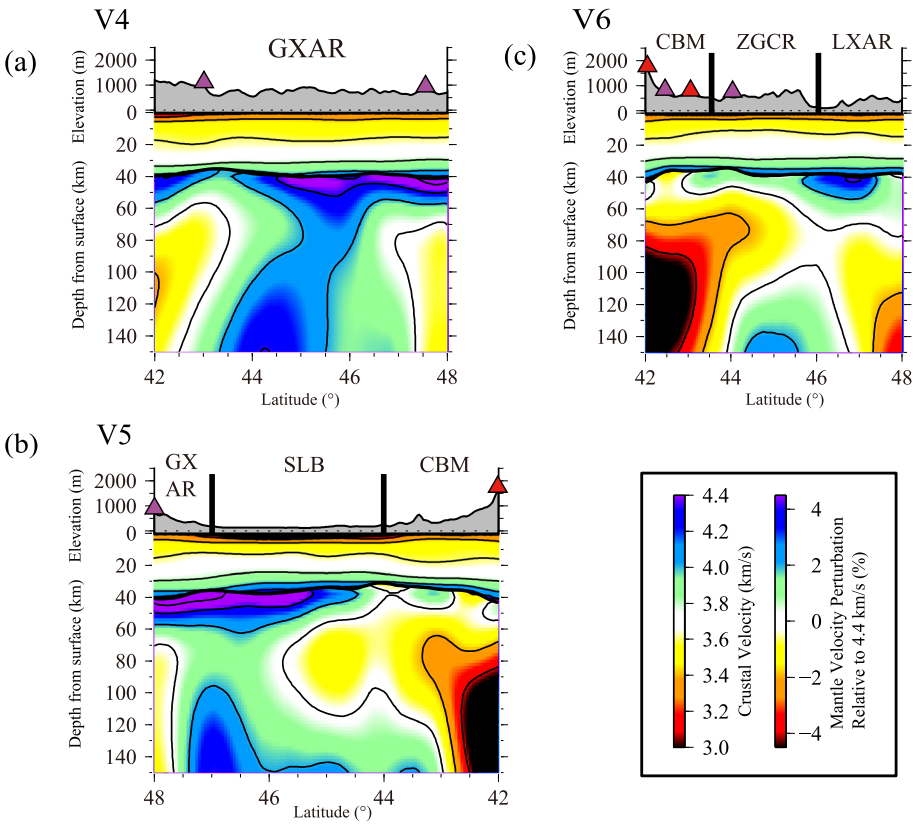

Figure 16. Three vertical transects (V4–V6, locations shown in Fig. 1b) through our V_s model plotted to 150 km with the same velocity scales as in Figs 13–15.

S-wave model produced by Tang *et al.* (2014), but there are differences in the vertical distribution of the imaged anomalies which are needed to fit the surface wave and RF data. In particular, we see a mantle lid beneath most of the study area and an enigmatic vertically arrayed 'fast-slow-fast' anomaly underlying the SLB at depths between 60 km and 100 km that deserves further investigation. This feature could be thermal in origin, caused by westward advective heating from the Lineated Volcanic Zone to the east or possibly by the onset of a top-down lithospheric instability or delamination. Alternately, the feature may reflect the crystal preferred orientation of anisotropic mantle minerals causing radial anisotropy that we are unable to resolve due to the absence of Love wave measurements.

The principal scientific motivation for this study is to investigate the expression of intracontinental volcanism in the crust and uppermost mantle beneath Northeast China. Beneath what we call the Northeast China Lineated Quaternary Volcanic Zone (Fig. 1a), we find the thinnest crust in the region as well as slow mid-crustal velocities. Low mantle shear wave speeds, however, principally underlie the southern part of this volcanic zone near Changbaishan Volcano, but do extend westward beneath much of the eastern SLB and appears as thin lithosphere. In contrast, the Northern and Southern Greater Xing'an Volcanic Zones (our terminology, Fig. 1a) display low velocity anomalies in both the crust and uppermost mantle but not crustal thinning. The central GXAR, which is well removed from Cenozoic volcanism, does not share the low mantle shear wave speeds found beneath the volcanic zones within the GXAR and the lithosphere is quite thick. The thin lithosphere beneath the Southern and Northern GXAR may coincide with the hypothesized previous episodes of delamination in the Mesozoic Era (Wang *et al.* 2006; Zhang *et al.* 2010) with later Cenozoic volcanism occurring only where thin lithosphere is present.

In the future, it would be beneficial to introduce Love waves in the analysis in order to investigate radial anisotropy in the crust and uppermost mantle. This may illuminate the so called fast-slow-fast mantle anomaly lying beneath the SLB, as this anomaly may result from the crystal preferred orientation of anisotropic minerals in the mantle. In addition, the strong similarity between the lateral distribution of depth-integrated velocity anomalies in the mantle between our model and the body wave model of Tang *et al.* (2014) calls for the joint inversion of our data together with teleseismic body wave data as done, for example, using USArray data by Obrebski *et al.* (2011) and by West *et al.* (2004) using RISTRA project data.

ACKNOWLEDGEMENTS

The authors are grateful to Steve Grand and an anonymous reviewer for insightful comments that improved this paper. DK and JN had extended work visits to the University of Colorado during which aspects of this work were completed, and they thank NSFC (41130316) for support. We thank all the people who participated in the NECESS Array project for installing/dismantling and servicing the seismic array. Aspects of this research were supported by NSF grant EAR-1246925 at the University of Colorado at Boulder. The facilities of IRIS Data Services, and specifically the IRIS Data Management Center, were used for access to waveforms, related metadata, and/or derived products used in this study. IRIS Data Services are funded through the Seismological Facilities for the Advancement of Geoscience and EarthScope (SAGE) Proposal

of the National Science Foundation under Cooperative Agreement EAR-1261681. This work utilized the Janus supercomputer, which is supported by the National Science Foundation (award number CNS-0821794), the University of Colorado at Boulder, the University of Colorado Denver and the National Center for Atmospheric Research. The Janus supercomputer is operated by the University of Colorado at Boulder.

REFERENCES

Bao, X., Song, X. & Li, J., 2015. High-resolution lithospheric structure beneath Mainland China from ambient noise and earthquake surface-wave tomography, *Earth planet. Sci. Lett.,* **417,** 132–141.

Barmin, M.P., Ritzwoller, M.H. & Levshin, A.L., 2001. A fast and reliable method for surface wave tomography, *Pure appl. Geophys.,* **158**(8), 1351–1375.

Bensen, G.D., Ritzwoller, M.H., Barmin, M.P., Levshin, A.L., Lin, F., Moschetti, M.P., Shapiro, N.M. & Yang, Y., 2007. Processing seismic ambient noise data to obtain reliable broad-band surface wave dispersion measurements, *Geophys. J. Int.,* **169,** 1239–1260.

Bodin, T., Sambridge, M., Tkalčić, H., Arroucau, P., Gallagher, K. & Rawlinson, N., 2012. Transdimensional inversion of receiver functions and surface wave dispersion, *J. geophys. Res.,* **117,** B02301, doi:10.1029/2011JB008560.

Boore, D.M. & Toksöz, M.N., 1969. Rayleigh wave particle motion and crustal structure, *Bull. seism. Soc. Am.,* **59**(1), 331–346.

Brocher, T.M., 2005. Empirical relations between elastic wavespeeds and density in the Earth's crust, *Bull. seism. Soc. Am.,* **95**(6), 2081–2092.

Chang, S.J., Baag, C.E. & Langston, C.A., 2004. Joint analysis of teleseismic receiver functions and surface wave dispersion using the genetic algorithm, *Bull. seism. Soc. Am.,* **94,** 691–704.

Chen, Y., Zhang, Y., Graham, D., Su, S. & Deng, J., 2007. Geochemistry of Cenozoic basalts and mantle xenoliths in Northeast China, *Lithos,* **96**(1–2), 108–126.

Chen, Z., Liu, G., Huang, Z., Lu, X., Luo, Q. & Ding, X., 2014. Controls of oil family distribution and composition in nonmarine petroleum systems: a case study from inner Mongolia Erlian basin, Northern China, *J. Asian Earth Sci.,* **92**, 36–52.

Dalton, C.A. & Ekstrom, G., 2006. Global models of surface wave attenuation, *J. geophys. Res.,* **111**(B10), 5317, doi:10.1029/2005JB003.

Feng, Z.Q., Jia, C.Z., Xie, X.N., Zhang, S., Feng, Z.H. & Timothy, A.C., 2010. Tectonostratigraphic units and stratigraphic sequences of the non-marine Songliao basin, northeast China, *Basin Res.,* **22,** 79–95.

Guo, Z. *et al.,* 2015. High resolution 3-D crustal structure beneath NE China from joint inversion of ambient noise and receiver functions using NECESSArray data, *Earth planet. Sci. Lett.,* **416,** 1–11.

Hacker, B.R. & Abers, G.A., 2004. Subduction Factory 3: An Excel worksheet and macro for calculating the densities, seismic wave speeds, and H2O contents of minerals and rocks at pressure and temperature, *Geochem. Geophys. Geosyst.,* **5,** Q01005, doi:10.1029/2003GC000614.

Huang, Z., Su, W., Peng, Y., Zheng, Y. & Li, H., 2003. Rayleigh wave tomography of China and adjacent regions, *J. geophys. Res.,* **108**(B2), 2073, doi:10.1029/2001JB001696.

Julià, J., Ammon, C.J., Herrmann, R.B. & Correig, A.M., 2000. Joint inversion of receiver function and surface wave dispersion observations, *Geophys. J. Int.,* **143,** 99–112.

Kanamori, H. & Anderson, D.L., 1977. Importance of physical dispersion in surface wave and free oscillation problems: Review, *Rev. Geophys.,* **15**(1), 105–112.

Kennett, B.L.N., Engdahl, E.R. & Buland, R., 1995. Constraints on seismic velocities in the earth from travel times, *Geophys. J. Int.,* **122,** 108–124

Li, Y., Wu, Q., Pan, J. & Sun, L., 2012. *S*-wave velocity structure of northeastern China from joint inversion of Rayleigh wave phase and group velocities, *Geophys. J. Int.,* **190**(1), 105–115.

Li, Y., Wu, Q., Pan, J., Zhang, F. & Yu, D., 2013. An upper-mantle *S*-wave velocity model for East Asia from Rayleigh wave tomography, *Earth planet. Sci. Lett.,* **377,** 367–377.

Ligorria, J.P. & Ammon, C.J., 1999. Iterative deconvolution and receiver-function estimation, *Bull. Seism. Soc. Am.,* **89,** 1395–400

Lin, F.-C. & Ritzwoller, M.H., 2011. Helmholtz surface wave tomography for isotropic and azimuthally anisotropic structure, *Geophys. J. Int.,* **186,** 1104–1120.

Lin, F.-C., Ritzwoller, M.H. & Snieder, R., 2009. Eikonal tomography: surface wave tomography by phase front tracking across a regional broadband seismic array, *Geophys. J. Int.,* **177,** 1091–1110.

Lin, F.-C., Schmandt, B. & Tsai, V.C., 2012. Joint inversion of Rayleigh wave phase velocity and ellipticity using USArray: constraining velocity and density structure in the upper crust, *Geophys. Res. Lett.,* **39,** L12303, doi:10.1029/2012GL052196.

Lin, F.-C., Tsai, V.C. & Schmandt, B., 2014. 3-D crustal structure of the western United States: application of Rayleigh-wave ellipticity extracted from noise cross-correlations, *Geophys. J. Int.,* **198**(2), 656–670.

Lin, Q., Ge, W.C., Sun, D.Y., Wu, F.Y., Chong, K.W., Kyung, D.M. & Sung, H.Y., 1998. Tectonic significance of Mesozoic volcanic rocks in northeastern China, *Sci. Geol. Sin.,* **33**(2), 129–138.

Liu, J.Q., Han, J.T. & Fyfe, W.S., 2001. Cenozoic episodic volcanism and continental rifting in northeast China and possible link to Japan Sea development as revealed from K–Ar geochronology, *Tectonophysics,* **339,** 385–401.

Mosegaard, K. & Tarantola, A., 1995. Monte Carlo sampling of solutions to inverse problems, *J. geophys. Res.,* **100**(B7), 12 431–12 447.

Niu, F. & Li, J., 2011. Component azimuths of the CEArray stations estimated from *P*-wave particle motion, *Earthq. Sci.,* **24**(1), 3–13.

Obrebski, M., Allen, R.M., Pollitz, F. & Hung, S.H., 2011. Lithosphere–asthenosphere interaction beneath the western United States from the joint inversion of body-wave traveltimes and surface-wave phase velocities, *Geophys. J. Int.,* **185**(2), 1003–1021.

Obrebski, M., Allen, R.M., Zhang, F., Pan, J., Wu, Q. & Hung, S.H., 2012. Shear wave tomography of China using joint inversion of body and surface wave constraints, *J. geophys. Res.,* **117**(B1), B01311, doi:10.1029/2011jb008349.

Ren, J., Tamaki, K, Li, S. & Zhang, J., 2002. Late Mesozoic and Cenozoic rifting and its dynamic setting in eastern China and adjacent areas, *Tectonophysics,* **344,** 175–205.

Schultz, C.A, Myers, S.C., Hipp, J & Young, C.J., 1998. Non-stationary Bayesian kriging: a predictive technique to generate spatial corrections for seismic detection, location and identification, *Bull. seism. Soc. Am.,* **88,** 1275–1288.

Shen, W., Ritzwoller, M.H., Schulte-Pelkum, V. & Lin, F.-C., 2013a. Joint inversion of surface wave dispersion and receiver functions: a Bayesian Monte-Carlo approach, *Geophys. J. Int.,* **192**(2), 807–836.

Shen, W., Ritzwoller, M.H. & Schulte-Pelkum, V., 2013b. A 3-D model of the crust and uppermost mantle beneath the Central and Western US by joint inversion of receiver functions and surface wave dispersion, *J. geophys. Res.,* **118**(1), 262–276.

Shen, W. *et al.,* 2015. A seismic reference model for the crust and uppermost mantle beneath China from surface wave dispersion, *Geophys. J. Int.,* in press.

Stepashko, A.A., 2006. The cretaceous dynamics of the pacific plate and stages of magmatic activity in Northeastern Asia, *Geotectonics,* **40**(3), 225–235.

Tang, Y. *et al.*, 2014. Changbaishan volcanism in northeast China linked to subduction induced mantle upwelling, *Nat. Geosci.,* **7,** 470–475.

Tanimoto, T. & Rivera, L., 2008. The ZH ratio method for long-period seismic data: sensitivity kernels and observational techniques, *Geophys. J. Int.,* **172,** 187–198.

Tao, K. *et al.,* 2014. Crustal structure beneath NE China imaged by NECESSArray receiver function data, *Earth planet. Sci. Lett.,* **398,** 48–57.

Wang, F., Zhou, X.H., Zhang, L.C., Ying, J.F., Zhang, Y.T., Wu, F.Y. & Zhu, R.X., 2006. Late Mesozoic volcanism in the Great Xing'an Range (NE China): timing and implications for the dynamic setting of NE Asia, *Earth planet. Sci. Lett.,* **251**(1), 179–198.

Wang, P.J., Xie, X., Mattern, F., Ren, Y., Zhu, D. & Sun, X., 2007. The Cretaceous Songliao Basin: volcanogenic succession, sedimentary sequence and tectonic evolution, NE China, *Acta Geol. Sin.,* **81,** 1002–1011.

Watson, M.P., Hayward, A.B., Parkinson, D.N. & Zhang, Z.M., 1987. Plate tectonic history, basin development and petroleum source rock deposition onshore China, *Mar. Pet. Geol.,* **4,** 205–225.

Wei, H.H., Liu, J.L. & Meng, Q.R., 2010. Structural and sedimentary evolution of the southern Songliao Basin, northeast China, and implications for hydrocarbon prospectivity, *AAPG Bull.,* **94**(4), 531–564.

West, M., Gao, W. & Grand, S., 2004. A simple approach to the joint inversion of seismic body and surface waves applied to the southwest U.S., *Geophys. Res. Lett.,* **31**(15), L15615, doi:10.1029/2004GL020373.

Wu, F., Jahn, B., Wilde, S.A., Lo, C., Yui, T., Lin, Q., Ge, W. & Sun, D., 2003a. Highly fractionated I-type granites in NE China (I): geochronology and petrogenesis, *Lithos,* **66**(3–4), 241–273.

Wu, F., Jahn, B., Wilde, S.A., Lo, C., Yui, T., Lin, Q., Ge, W. & Sun, D., 2003b. Highly fractionated I-type granites in NE China (II): isotopic geochemistry and implications for crustal growth in the Phanerozoic, *Lithos,* **67**(3–4), 191–204

Wu, F.Y., Sun, D.Y., Ge, W.C., Zhang, Y.B., Grant, M.L., Wilde, S.A. & Jahn, B.M., 2011. Geochronology of the Phanerozoic granitoids in northeastern China, *J. Asian Earth Sci.,* **41,** 1–30.

Xie, J., Ritzwoller, M.H., Brownlee, S. & Hacker, B., 2015. Inferring the oriented elastic tensor from surface wave observations: preliminary application across the Western US, *Geophys. J. Int.,* **201,** 996–1021.

Yang, Y. *et al.*, 2010. Rayleigh wave phase velocity maps of Tibet and the surrounding regions from ambient seismic noise tomography, *Geochem. Geophys. Geosys.,* **11**(8), Q08010, doi:10.1029/2010GC003119.

Yang, Y., Ritzwoller, M.H., Zheng, Y., Shen, W., Levshin, A.L. & Xie, Z., 2012. A synoptic view of the distribution and connectivity of the mid-crustal low velocity zone beneath Tibet, *J. geophys. Res.,* **117**(B4), B04303, doi:10.1029/2011JB008810.

Yano, T., Tanimoto, T. & Rivera, L., 2009. The ZH ratio method for long-period seismic data: inversion for *S*-wave velocity structure, *Geophys. J. Int.,* **179,** 413–424.

Zhang, F.Q., Chen, H.L., Yu, X., Dong, C.W., Yang, S.F., Pang, Y.M. & Batt, G.E., 2011. Early Cretaceous volcanism in the northern Songliao Basin, NE China, and its geodynamic implication, *Gondwana Res.,* **19** (1), 163–176.

Zhang, F.-Q, Chen, H.-L. & Yang, S.-F., 2012. Late Mesozoic-Cenozoic evolution of the Sanjiang Basin in NE China and its tectonic implications for the West Pacific continental margin, *J. Asian Earth Sci.,* **49,** 287–299.

Zhang, J.H., Gao, S., Ge, W.C., Wu, F.Y., Yang, J.H., Wilde, S.A. & Li, M., 2010. Geochronology of the Mesozoic volcanic rocks in the Great Xing'an Range, northeastern China: implications for subduction-induced delamination, *Chem. Geol.,* **276**(3), 144–165.

Zheng, S., Sun, X., Song, X., Yang, Y. & Ritzwoller, M.H., 2008. Surface wave tomography of China from ambient seismic noise correlation, *Geochem. Geophys. Geosyst.,* **9**(5), doi:10.1029/2008GC001981.

Zheng, Y., Shen, W., Zhou, L., Yang, Y., Xie, Z. & Ritzwoller, M.H., 2011. Crust and uppermost mantle beneath the North China Craton, northeastern China, and the Sea of Japan from ambient noise tomography, *J. geophys. Res.,* **116,** B12312, doi:10.1029/2011JB008637.

Zhou, L., Xie, J., Shen, W., Zheng, Y., Yang, Y., Shi, H. & Ritzwoller, M.H. 2012. The structure of the crust and uppermost mantle beneath South China from ambient noise and earthquake tomography, *Geophys. J. Int.,* doi:10.1111/j.1365-246X.2012.05423.x.